

GAS SEPARATION

Ethane/ethylene separation in a metal-organic framework with iron-peroxo sites

Libo Li^{1,2,6*}, Rui-Biao Lin^{2*}, Rajamani Krishna³, Hao Li^{2,4}, Shengchang Xiang⁴, Hui Wu⁵, Jinping Li^{1,6†}, Wei Zhou^{5†}, Banglin Chen^{2†}

The separation of ethane from its corresponding ethylene is an important, challenging, and energy-intensive process in the chemical industry. Here we report a microporous metal-organic framework, iron(III) peroxide 2,5-dioxido-1,4-benzenedicarboxylate [$\text{Fe}_2(\text{O}_2)(\text{dobdc})$ (dobdc^4 : 2,5-dioxido-1,4-benzenedicarboxylate)], with iron (Fe)-peroxo sites for the preferential binding of ethane over ethylene and thus highly selective separation of $\text{C}_2\text{H}_6/\text{C}_2\text{H}_4$. Neutron powder diffraction studies and theoretical calculations demonstrate the key role of Fe-peroxo sites for the recognition of ethane. The high performance of $\text{Fe}_2(\text{O}_2)(\text{dobdc})$ for the ethane/ethylene separation has been validated by gas sorption isotherms, ideal adsorbed solution theory calculations, and simulated and experimental breakthrough curves. Through a fixed-bed column packed with this porous material, polymer-grade ethylene (99.99% pure) can be straightforwardly produced from ethane/ethylene mixtures during the first adsorption cycle, demonstrating the potential of $\text{Fe}_2(\text{O}_2)(\text{dobdc})$ for this important industrial separation with a low energy cost under ambient conditions.

Ethylene (C_2H_4) is the largest feedstock in petrochemical industries, with a global production capacity of more than 170 million tons in 2016. It is usually produced by steam cracking or thermal decomposition of ethane (C_2H_6), in which a certain amount of C_2H_6 residue coexists in the product and needs to be removed to produce polymer-grade ($\geq 99.95\%$ pure) C_2H_4 as the starting chemical for many other products, particularly the widely utilized polyethylene. The well-established industrial separation technology of the cryogenic high-pressure distillation process is one of the most energy-intensive processes in the chemical industry, requiring large distillation columns with 120 to 180 trays and high reflux ratios because of the similar sizes and volatilities of C_2H_4 and C_2H_6 (1, 2). Realization of cost- and energy-efficient $\text{C}_2\text{H}_4/\text{C}_2\text{H}_6$ separation to obtain polymer-grade C_2H_4 is highly desired and has been recently highlighted as one of the most important industrial separation tasks for future energy-efficient separation processes (3–5).

Adsorbent-based gas separation, through pressure swing adsorption (PSA), temperature swing

adsorption, or membranes, is a promising technology to replace the traditional cryogenic distillation and thus to fulfill the energy-efficient separation economy. Some adsorbents, such as $\gamma\text{-Al}_2\text{O}_3$ (6), zeolite (7, 8), and metal-organic frameworks (MOFs) (9, 10), have been developed for $\text{C}_2\text{H}_4/\text{C}_2\text{H}_6$ adsorptive separation. These porous materials take up larger amounts of C_2H_4 than of C_2H_6 , mainly because of the stronger interactions of the immobilized metal sites, such as Ag(I) and Fe(II), on the pore surfaces with unsaturated C_2H_4 molecules (9, 11). Although these kinds of adsorbents exhibit excellent adsorption

separation performance toward $\text{C}_2\text{H}_4/\text{C}_2\text{H}_6$ mixtures, with the selectivity up to 48.7 (12), production of high-grade C_2H_4 is still quite energy intensive. This is because C_2H_4 , as the preferentially adsorbed gas, needs to be further desorbed to get the C_2H_4 product. To remove the unadsorbed and contaminated C_2H_6 , at least four adsorption-desorption cycles through inert gas or a vacuum pump are necessary to achieve the purity limit required ($\geq 99.95\%$) for the C_2H_4 polymerization reactor (13).

If C_2H_6 is preferentially adsorbed, the desired C_2H_4 product can be directly recovered in the adsorption cycle. Compared with C_2H_4 -selective adsorbents, this approach can save approximately 40% of energy consumption (0.4 to 0.6 GJ/ton of ethylene) (14, 15) on PSA technology for the $\text{C}_2\text{H}_6/\text{C}_2\text{H}_4$ separation. Although porous materials have been well established for gas separation and purification (16–22), those exhibiting the preferred C_2H_6 adsorption over C_2H_4 are scarce. To date, only a few porous materials for selective $\text{C}_2\text{H}_6/\text{C}_2\text{H}_4$ separation have been reported (2, 13, 23, 24), with quite low separation selectivity and productivity.

To target MOFs with the preferential binding of C_2H_6 over C_2H_4 , it is necessary to immobilize some specific sites for the stronger interactions with C_2H_6 . Inspired by natural metalloenzymes and synthetic compounds for alkane C–H activation in which M-peroxo, M-hydroperoxo, and M-oxo [M = Cu(II), Co(III), and Fe (III/IV)] are active catalytic intermediates (25–27), we hypothesized that similar functional sites within MOFs might have stronger binding with alkanes than alkenes and thus could be utilized for the selective separation of $\text{C}_2\text{H}_6/\text{C}_2\text{H}_4$. In this regard, $\text{Fe}_2(\text{O}_2)(\text{dobdc})$, developed by Bloch *et al.* and containing iron(III)-peroxo sites on the pore surfaces, might be of special interest (28, 29). We thus synthesized the $\text{Fe}_2(\text{O}_2)(\text{dobdc})$, studied its binding for C_2H_6 ,

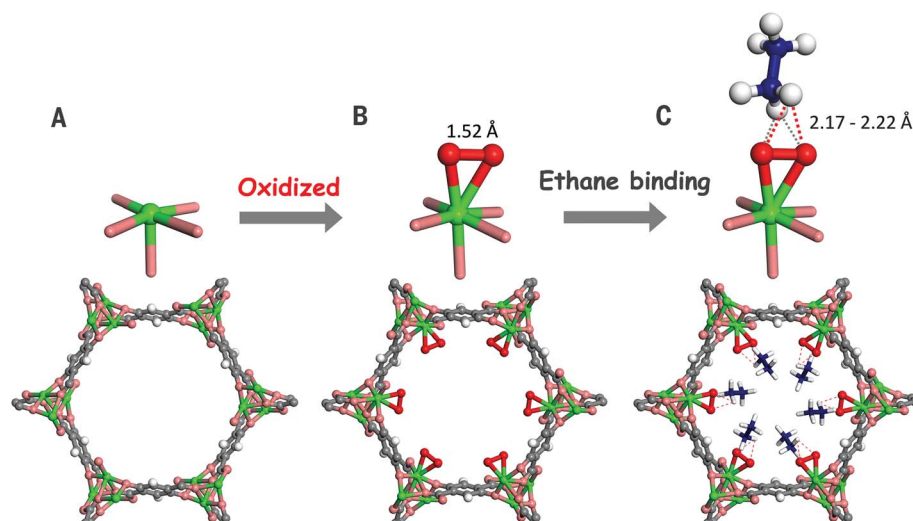


Fig. 1. Structures determined from NPD studies. Shown are structures of (A) $\text{Fe}_2(\text{dobdc})$, (B) $\text{Fe}_2(\text{O}_2)(\text{dobdc})$, and (C) $\text{Fe}_2(\text{O}_2)(\text{dobdc})\text{C}_2\text{D}_6$ at 7 K. Note the change from the open Fe(II) site to the Fe(III)-peroxo site for the preferential binding of ethane. Fe, green; C, dark gray; O, pink; O^{2-} , red; H or D, white; C in C_2D_6 , blue.

and examined the separation performance for $\text{C}_2\text{H}_6/\text{C}_2\text{H}_4$ mixtures. We found that $\text{Fe}_2(\text{O}_2)(\text{dobdc})$ exhibits preferential binding of C_2H_6 over C_2H_4 . $\text{Fe}_2(\text{O}_2)(\text{dobdc})$ not only takes up moderately high amounts of C_2H_6 but also displays the highest $\text{C}_2\text{H}_6/\text{C}_2\text{H}_4$ separation selectivities in the wide pressure range among the examined porous materials, demonstrating it as the best material reported to date for this important gas separation to produce polymer-grade ethylene (99.99% pure).

$\text{Fe}_2(\text{O}_2)(\text{dobdc})$ was prepared according to the previously reported procedure with a slight modification (28). Both $\text{Fe}_2(\text{dobdc})$ and $\text{Fe}_2(\text{O}_2)(\text{dobdc})$ are air sensitive and need to be handled and stored in a dry box under an N_2 atmosphere. As expected, $\text{Fe}_2(\text{O}_2)(\text{dobdc})$ maintains the framework structure of $\text{Fe}_2(\text{dobdc})$ (Fig. 1, A and B, and fig. S1A), with a Brunauer-Emmett-Teller surface area of $1073 \text{ m}^2/\text{g}$ (fig. S1B).

The C_2H_6 binding affinity in $\text{Fe}_2(\text{O}_2)(\text{dobdc})$ was first investigated by single-component sorption isotherms at a temperature of 298 K and pressures up to 1 bar, as shown in Fig. 2A. The C_2H_6 adsorption capacity on $\text{Fe}_2(\text{O}_2)(\text{dobdc})$ is much higher than that of C_2H_4 , implying the distinct binding affinity of $\text{Fe}_2(\text{O}_2)(\text{dobdc})$ for C_2H_6 . At 1 bar, the uptake amount of C_2H_6 in

$\text{Fe}_2(\text{O}_2)(\text{dobdc})$ is $74.3 \text{ cm}^3/\text{g}$, corresponding to $\sim 1.1 \text{ C}_2\text{H}_6$ per $\text{Fe}_2(\text{O}_2)(\text{dobdc})$ formula. Unlike the pristine $\text{Fe}_2(\text{dobdc})$, which takes up more C_2H_4 than C_2H_6 because of the Fe(II) open sites, $\text{Fe}_2(\text{O}_2)(\text{dobdc})$ adsorbs a larger amount of C_2H_6 than of C_2H_4 . Therefore, we successfully realized the “reversed $\text{C}_2\text{H}_6/\text{C}_2\text{H}_4$ adsorption” in $\text{Fe}_2(\text{O}_2)(\text{dobdc})$ (fig. S2). The adsorption heats (Q_{st}) of C_2H_6 and C_2H_4 on $\text{Fe}_2(\text{O}_2)(\text{dobdc})$ were calculated by using the virial equation (fig. S3). The C_2H_6 adsorption heat of $\text{Fe}_2(\text{O}_2)(\text{dobdc})$ was calculated to be 66.8 kJ/mol at zero coverage, a much higher value than those reported for other MOFs (2), indicating the strong interaction between $\text{Fe}_2(\text{O}_2)(\text{dobdc})$ and C_2H_6 molecules. All of the isotherms are completely reversible and exhibit no hysteresis. Further adsorption cycling tests at 298 K (fig. S4) indicated no loss of C_2 uptake capacity over 20 adsorption-desorption cycles.

To structurally elucidate how C_2H_6 and C_2H_4 are adsorbed in this MOF, high-resolution neutron powder diffraction (NPD) measurements were carried out on C_2D_6 -loaded and C_2D_4 -loaded samples of $\text{Fe}_2(\text{O}_2)(\text{dobdc})$ at 7 K (see supplementary materials and fig. S5). As shown in Fig. 1C, C_2D_6 molecules exhibit preferential binding with the peroxy sites through C–D···O hydrogen

bonds (D···O, ~ 2.17 to 2.22 \AA). The D···O distance is much shorter than the sum of van der Waals radii of oxygen (1.52 \AA) and hydrogen (1.20 \AA) atoms, indicating a relatively strong interaction, which is consistent with the high C_2H_6 adsorption heat found in $\text{Fe}_2(\text{O}_2)(\text{dobdc})$. In addition, we noticed that, sterically, the nonplanar C_2D_6 molecule happens to match better to the uneven pore surface in $\text{Fe}_2(\text{O}_2)(\text{dobdc})$ than the planar C_2D_4 molecule (fig. S6), resulting in stronger hydrogen bonds with the Fe-peroxo active site and stronger van der Waals interactions with the ligand surface. To further understand the mechanism of the selective $\text{C}_2\text{H}_6/\text{C}_2\text{H}_4$ adsorption in $\text{Fe}_2(\text{O}_2)(\text{dobdc})$, we conducted detailed first-principles dispersion-corrected density functional theory calculations (see supplementary materials and table S1). The optimized C_2H_6 binding configuration on the Fe-peroxo site agrees reasonably well with the C_2D_6 -loaded structures determined from the NPD data, indicating that the reversed $\text{C}_2\text{H}_6/\text{C}_2\text{H}_4$ adsorption selectivity originates from the peroxy active sites and the electronegative surface oxygen distribution in $\text{Fe}_2(\text{O}_2)(\text{dobdc})$. Similar preferential binding of C_2H_6 over C_2H_4 has also been experimentally found in another oxidized MOF, Cr-BTC(O_2) (where BTC is 1,3,5-benzenetricarboxylate) (figs. S7 and S8) (30).

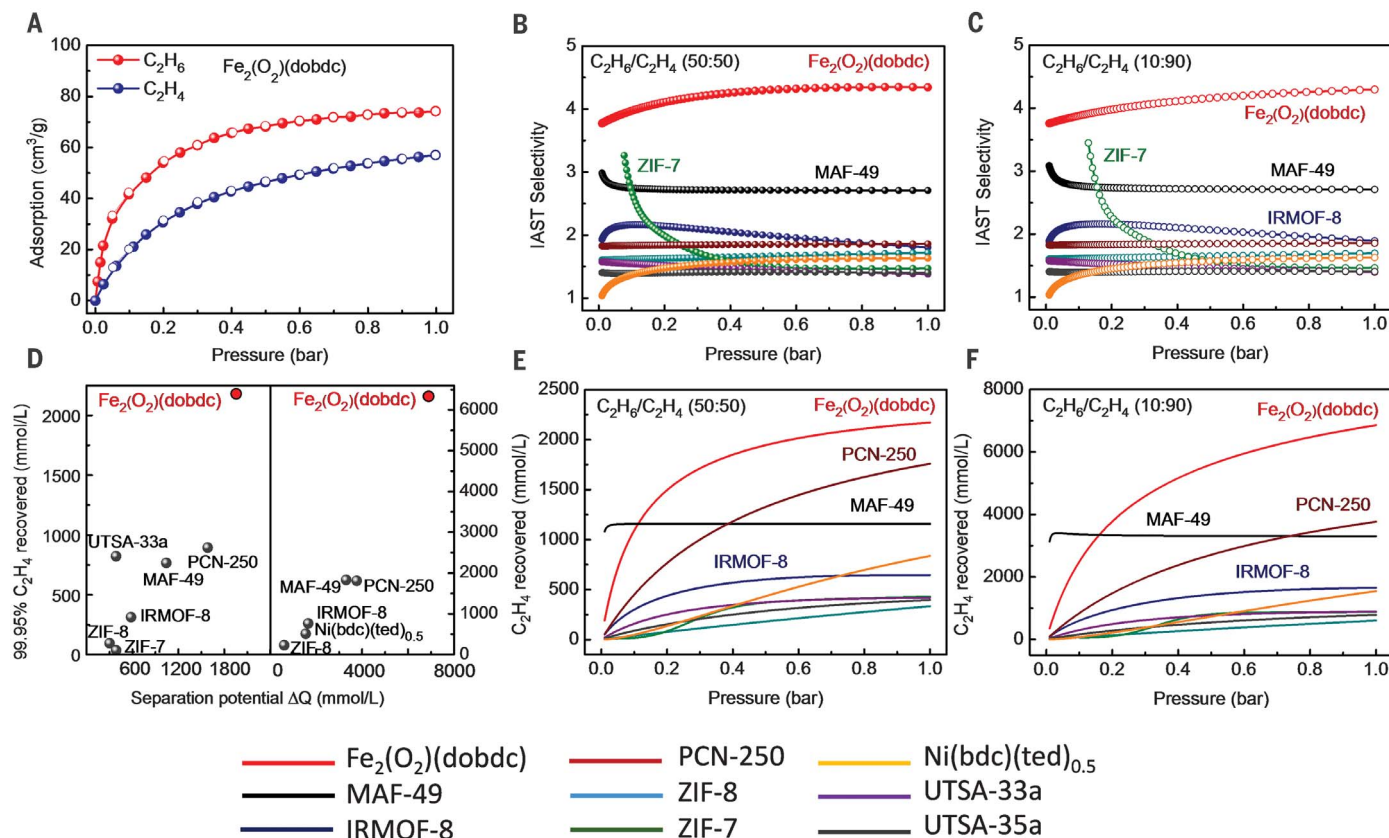


Fig. 2. C_2H_6 and C_2H_4 adsorption isotherms of $\text{Fe}_2(\text{O}_2)(\text{dobdc})$, IAST calculations, and separation potential simulations on C_2H_6 -selective MOFs. (A) Adsorption (solid) and desorption (open) isotherms of C_2H_6 (red circles) and C_2H_4 (blue circles) in $\text{Fe}_2(\text{O}_2)(\text{dobdc})$ at 298 K. **(B and C)** Comparison of the IAST selectivities of $\text{Fe}_2(\text{O}_2)(\text{dobdc})$ with those of previously reported best-performing materials for $\text{C}_2\text{H}_6/\text{C}_2\text{H}_4$ (50/50 and 10/90) mixtures. **(D)** Predicted productivity of 99.95% pure C_2H_6 from $\text{C}_2\text{H}_6/\text{C}_2\text{H}_4$ (50/50 and 10/90) mixtures in fixed-bed adsorbers at 298 K. **(E and F)** Separation potential of $\text{Fe}_2(\text{O}_2)(\text{dobdc})$ for $\text{C}_2\text{H}_6/\text{C}_2\text{H}_4$ [50/50 (E) and 10/90 (F)] mixtures versus those of best-performing MOFs.

Ideal adsorbed solution theory (IAST) calculations were performed to estimate the adsorption selectivities of $\text{C}_2\text{H}_6/\text{C}_2\text{H}_4$ (50/50 and 10/90) for $\text{Fe}_2(\text{O}_2)(\text{dobdc})$ and other C_2H_6 -selective materials (Fig. 2B). The fitting details are provided in the supplementary materials (figs. S9 to S17 and tables S2 to S11). Compared with other top-performing MOFs [MAF-49, IRMOF-8, ZIF-8, ZIF-7, PCN-250, Ni(bdc)(ted)_{0.5}, UTSA-33a, and UTSA-35a], $\text{Fe}_2(\text{O}_2)(\text{dobdc})$ exhibits a new benchmark for $\text{C}_2\text{H}_6/\text{C}_2\text{H}_4$ (50/50) adsorption selectivity (4.4) at 1 bar and 298 K, greater than the selectivity of the previously reported best-performing MOF, MAF-49 (2.7) (2). This value is also higher than the highest value (2.9) among 30,000 all-silica zeolite structures that were investigated by Kim *et al.* through computational screening (31). For a $\text{C}_2\text{H}_6/\text{C}_2\text{H}_4$ (10/90) mixture, under the same conditions, $\text{Fe}_2(\text{O}_2)(\text{dobdc})$ also exhibits the highest adsorption selectivity among these MOFs (Fig. 2C).

Next, transient breakthrough simulations were conducted to validate the feasibility of using $\text{Fe}_2(\text{O}_2)(\text{dobdc})$ in a fixed bed for separation of $\text{C}_2\text{H}_6/\text{C}_2\text{H}_4$ mixtures (fig. S18). Two $\text{C}_2\text{H}_6/\text{C}_2\text{H}_4$ mixtures (50/50 and 10/90) were used as feeds to mimic the industrial process conditions. The simulated breakthrough curves show that $\text{C}_2\text{H}_6/\text{C}_2\text{H}_4$ (50/50) mixtures were completely separated by $\text{Fe}_2(\text{O}_2)(\text{dobdc})$, whereby C_2H_4 breakthrough occurred first within seconds to yield the polymer-grade gas and then C_2H_6 passed through the fixed bed after a certain time (τ_{break}). To evaluate the $\text{C}_2\text{H}_6/\text{C}_2\text{H}_4$ separation ability of these MOFs, the separation potential ΔQ was calculated to quantify the mixture separations in fixed-bed adsorbents (table S12). Attributed to the record-high $\text{C}_2\text{H}_6/\text{C}_2\text{H}_4$ selectivity and relatively high C_2H_6 uptake, the amount of 99.95% pure C_2H_4 recovered by $\text{Fe}_2(\text{O}_2)(\text{dobdc})$ reached up to 2172 mmol/liter ($\text{C}_2\text{H}_6/\text{C}_2\text{H}_4$, 50/50) and 6855 mmol/liter ($\text{C}_2\text{H}_6/\text{C}_2\text{H}_4$, 10/90) (Fig. 2D), values which are almost two times higher than those for the other benchmark materials. $\text{Fe}_2(\text{O}_2)(\text{dobdc})$ has the highest separation potential for recovering the pure C_2H_4 from (50/50) $\text{C}_2\text{H}_6/\text{C}_2\text{H}_4$ mixtures during the adsorption process (Fig. 2E). Even when the concentration of C_2H_6 decreases to 10% (Fig. 2F), $\text{Fe}_2(\text{O}_2)(\text{dobdc})$ maintains the highest separation potential (table S13), which makes it the most promising material for the separation of C_2H_6 from $\text{C}_2\text{H}_6/\text{C}_2\text{H}_4$ mixtures.

These excellent breakthrough results from simulation encouraged us to further evaluate the separation performance of $\text{Fe}_2(\text{O}_2)(\text{dobdc})$ in the actual separation process. Several breakthrough experiments were performed on an in-house-constructed apparatus, which was described in our previous work (32). The breakthrough experiments were performed on several selected MOFs, including $\text{Fe}_2(\text{O}_2)(\text{dobdc})$, with $\text{C}_2\text{H}_6/\text{C}_2\text{H}_4$ (50/50) mixtures flowed over a packed bed at a total flow rate of 5 ml/min at 298 K (fig. S19 and table S14). For $\text{Fe}_2(\text{O}_2)(\text{dobdc})$, a clean and sharp separation of $\text{C}_2\text{H}_6/\text{C}_2\text{H}_4$ was observed (Fig. 3A). C_2H_4 was first to elute through the bed, before it was contaminated with undetectable amounts of C_2H_6 , resulting in a high

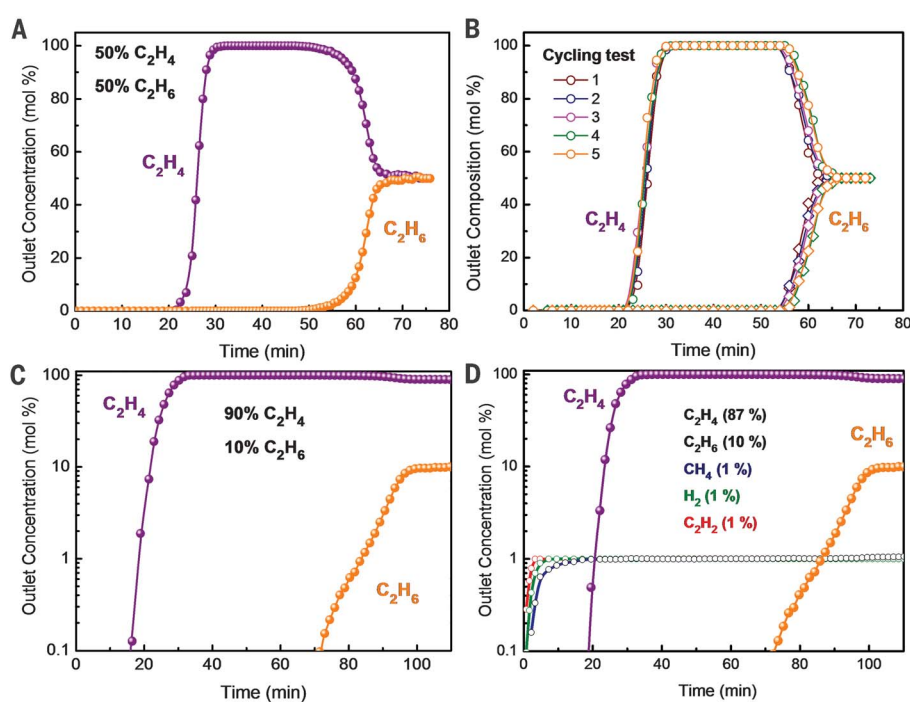


Fig. 3. Breakthrough experiments. Experimental column breakthrough curves for (A) a $\text{C}_2\text{H}_6/\text{C}_2\text{H}_4$ (50/50) mixture, (B) a cycling test of $\text{C}_2\text{H}_6/\text{C}_2\text{H}_4$ (50/50) mixtures, (C) $\text{C}_2\text{H}_6/\text{C}_2\text{H}_4$ (10/90) mixtures, and (D) $\text{C}_2\text{H}_6/\text{C}_2\text{H}_4/\text{C}_2\text{H}_2/\text{CH}_4/\text{H}_2$ (10/87/1/1/1) mixtures in an absorber bed packed with $\text{Fe}_2(\text{O}_2)(\text{dobdc})$ at 298 K and 1.01 bar.

concentration of C_2H_4 feed that was $\geq 99.99\%$ pure (the detection limit of the instrument is 0.01%). After some period, the adsorbent got saturated, C_2H_6 broke through, and then the outlet gas stream quickly reached equimolar concentrations. To make the systematic comparison for the C_2H_4 separation performance in the selected MOFs, C_2H_4 purity and productivity were calculated from their breakthrough curves (table S15). For $\text{Fe}_2(\text{O}_2)(\text{dobdc})$, 0.79 mmol/g of C_2H_4 with $\geq 99.99\%$ purity can be recovered from the $\text{C}_2\text{H}_4/\text{C}_2\text{H}_6$ (50/50) mixture in a single breakthrough operation; this value is nearly three times that for the benchmark material MAF-49 (0.28 mmol/g). In addition, the cycle and regeneration capabilities of $\text{Fe}_2(\text{O}_2)(\text{dobdc})$ were further studied by breakthrough cycle experiments (Fig. 3B), with no noticeable decrease in the mean residence times for both C_2H_6 and C_2H_4 within five continuous cycles under ambient conditions. Moreover, $\text{Fe}_2(\text{O}_2)(\text{dobdc})$ material retained its stability after the breakthrough cycling test (fig. S20).

In the real production of high-purity C_2H_4 , the C_2H_6 concentration in $\text{C}_2\text{H}_4/\text{C}_2\text{H}_6$ mixtures produced by naphtha cracking is about 6 to 10%, and the feed gases are also contaminated by low levels of impurities such as CH_4 , H_2 , and C_2H_2 (33). Therefore, breakthrough experiments on $\text{C}_2\text{H}_6/\text{C}_2\text{H}_4$ (10/90) mixtures and $\text{C}_2\text{H}_6/\text{C}_2\text{H}_4/\text{CH}_4/\text{H}_2/\text{C}_2\text{H}_2$ (10/87/1/1/1) mixtures were also performed for $\text{Fe}_2(\text{O}_2)(\text{dobdc})$. As shown in Fig. 3, C and D, highly efficient separations for both mixtures were realized, which further demon-

strates that $\text{Fe}_2(\text{O}_2)(\text{dobdc})$ can be used to purify C_2H_4 with low concentrations of C_2H_6 even in the presence of CH_4 , H_2 , and C_2H_2 impurities.

In summary, we discovered that a distinctive MOF with Fe-peroxo sites can induce stronger interactions with C_2H_6 than with C_2H_4 , leading to the unusual reversed $\text{C}_2\text{H}_6/\text{C}_2\text{H}_4$ adsorption. The fundamental binding mechanism of $\text{Fe}_2(\text{O}_2)(\text{dobdc})$ for the recognition of C_2H_6 has been demonstrated through neutron diffraction studies and theoretical calculations, indicating the important role of the Fe-peroxo sites for the preferential interactions with C_2H_6 . This material can readily produce high-purity C_2H_4 ($\geq 99.99\%$ pure) from $\text{C}_2\text{H}_4/\text{C}_2\text{H}_6$ mixtures during the first breakthrough cycle with moderately high productivity and a low energy cost. The strategy we developed in this work may be broadly applicable, which will facilitate extensive research on the immobilization of different sites into porous MOFs for stronger interactions with C_2H_6 than with C_2H_4 , thus targeting some practically useful porous materials with low material costs and high productivity for the practical industrial realization of this very challenging and important separation.

REFERENCES AND NOTES

1. F. Bander, Separation Technologies; <http://seperationtechnology.com>.
2. P.-Q. Liao, W.-X. Zhang, J.-P. Zhang, X.-M. Chen, *Nat. Commun.* **6**, 8697 (2015).
3. D. S. Sholl, R. P. Lively, *Nature* **532**, 435–437 (2016).
4. J. Y. S. Lin, *Science* **353**, 121–122 (2016).
5. S. Chu, Y. Cui, N. Liu, *Nat. Mater.* **16**, 16–22 (2016).

6. R. T. Yang, E. S. Kikkilides, *AIChE J.* **41**, 509–517 (1995).
7. P. J. Bereciartua et al., *Science* **358**, 1068–1071 (2017).
8. S. Aguado, G. Bergeret, C. Daniel, D. Farrusseng, *J. Am. Chem. Soc.* **134**, 14635–14637 (2012).
9. E. D. Bloch et al., *Science* **335**, 1606–1610 (2012).
10. Y. He, R. Krishna, B. Chen, *Energy Environ. Sci.* **5**, 9107–9120 (2012).
11. B. Li et al., *J. Am. Chem. Soc.* **136**, 8654–8660 (2014).
12. S. Yang et al., *Nat. Chem.* **7**, 121–129 (2015).
13. C. Güçyener, J. van den Bergh, J. Gascon, F. Kapteijn, *J. Am. Chem. Soc.* **132**, 17704–17706 (2010).
14. A. Mersmann, B. Fill, R. Hartmann, S. Maurer, *Chem. Eng. Technol.* **23**, 937–944 (2000).
15. T. Ren, M. Patel, K. Blok, *Energy* **31**, 425–451 (2006).
16. H. Furukawa, K. E. Cordova, M. O’Keeffe, O. M. Yaghi, *Science* **341**, 1230444 (2013).
17. H. Sato et al., *Science* **343**, 167–170 (2014).
18. A. Cadiau, K. Adil, P. M. Bhatt, Y. Belmabkhout, M. Eddaoudi, *Science* **353**, 137–140 (2016).
19. R. Vaidhyanathan et al., *Science* **330**, 650–653 (2010).
20. P. Nugent et al., *Nature* **495**, 80–84 (2013).
21. Q.-G. Zhai et al., *Nat. Commun.* **7**, 13645 (2016).
22. K. Li et al., *J. Am. Chem. Soc.* **131**, 10368–10369 (2009).
23. W. Liang et al., *Chem. Eng. Sci.* **148**, 275–281 (2016).
24. Y. Chen et al., *Chem. Eng. Sci.* **175**, 110–117 (2018).
25. D. J. Xiao et al., *Nat. Chem.* **6**, 590–595 (2014).
26. Z. Li et al., *J. Am. Chem. Soc.* **139**, 15251–15258 (2017).
27. J. Cho et al., *Nature* **478**, 502–505 (2011).
28. E. D. Bloch et al., *J. Am. Chem. Soc.* **133**, 14814–14822 (2011).
29. W. L. Queen et al., *Dalton Trans.* **41**, 4180–4187 (2012).
30. L. J. Murray et al., *J. Am. Chem. Soc.* **132**, 7856–7857 (2010).
31. J. Kim et al., *Langmuir* **28**, 11914–11919 (2012).
32. L. Li et al., *J. Am. Chem. Soc.* **139**, 7733–7736 (2017).
33. R. A. Meyers, *Handbook of Petrochemicals Production Processes* (McGraw-Hill, 2005).

ACKNOWLEDGMENTS

L.L. and R.-B.L. thank B. Li for the discussions on this project and S. Li for preparation of breakthrough experiments. **Funding:** We gratefully acknowledge the financial support from the National Natural Science Foundation of China (2160163), the Natural Science Foundation of Shanxi (201601D021042), and the Welch Foundation (AX-1730). **Author contributions:** L.L., R.-B.L., J.L., W.Z., and B.C. conceived the idea and designed the experiments. L.L. synthesized the materials and carried out most of the

adsorption and separation experiments. H.L. and S.X. prepared the samples and analyzed the data. R.K. calculated the IAST selectivity and performed the simulated breakthrough. L.L., W.Z., and H.W. carried out the NPD experiments and analyzed the results. L.L., R.-B.L., W.Z., and B.C. interpreted the results and wrote the paper. **Competing interests:** None declared. **Data and materials availability:** Crystallographic data reported in this paper are provided in the supplementary materials and archived at the Cambridge Crystallographic Data Centre under reference numbers 1817715 to 1817716, 1574716 to 1574717, and 1859806 to 1859808. All other data needed to evaluate the conclusions in the paper are present in the paper or the supplementary materials.

SUPPLEMENTARY MATERIALS

www.science.org/content/362/6413/443/suppl/DC1
Materials and Methods
Figs. S1 to S20
Tables S1 to S15
References (34–40)
19 January 2018; resubmitted 8 June 2018
Accepted 5 September 2018
10.1126/science.aat0586

Ethane/ethylene separation in a metal-organic framework with iron-peroxo sites

Libo Li, Rui-Biao Lin, Rajamani Krishna, Hao Li, Shengchang Xiang, Hui Wu, Jinping Li, Wei Zhou and Banglin Chen

Science 362 (6413), 443-446.
DOI: 10.1126/science.aat0586

A preference for ethane

Industrial production of ethylene requires its separation from ethane in a cryogenic process that consumes large amounts of energy. An alternative would be differential sorption in microporous materials. Most of these materials bind ethylene more strongly than ethane, but adsorption of ethane would be more efficient. Li *et al.* found that a metal-organic framework containing iron-peroxo sites bound ethane more strongly than ethylene and could be used to separate the gases at ambient conditions.

Science, this issue p. 443

ARTICLE TOOLS

<http://science.scienmag.org/content/362/6413/443>

SUPPLEMENTARY MATERIALS

<http://science.scienmag.org/content/suppl/2018/10/24/362.6413.443.DC1>

REFERENCES

This article cites 38 articles, 7 of which you can access for free
<http://science.scienmag.org/content/362/6413/443#BIBL>

PERMISSIONS

<http://www.scienmag.org/help/reprints-and-permissions>

Use of this article is subject to the [Terms of Service](#)

Supplementary Materials for

Ethane/ethylene separation in a metal-organic framework with iron-peroxo sites

Libo Li,* Rui-Biao Lin,* Rajamani Krishna, Hao Li, Shengchang Xiang, Hui Wu,
Jinping Li,† Wei Zhou,† Banglin Chen†

*These authors contributed equally to this work.

†Corresponding author. Email: jpli211@hotmail.com (J.L.); wzhou@nist.gov (W.Z.);
banglin.chen@utsa.edu (B.C.)

Published 26 October 2018, *Science* **362**, 443 (2018)
DOI: 10.1126/science.aat0586

This PDF file includes:

Materials and Methods
Figs. S1 to S20
Tables S1 to S15
References

Materials and Methods

Materials

Anhydrous ferrous chloride (FeCl₂, 98%, Aldrich), 2,5-dihydroxyterephthalic acid (98%, Aldrich), N,N-dimethylformamide, (DMF, anhydrous, 99.8%, Sigma-Aldrich), methanol (CH₃OH, anhydrous, 99.8%, Sigma-Aldrich) were purchased and used without further purification.

N₂ (99.999%), O₂ (99.999%), C₂H₄ (99.99%), C₂H₆ (99.99%), He (99.999%) and mixed gases of (1) C₂H₆/C₂H₄ = 50/50 (v/v), (2) C₂H₆/C₂H₄ = 10/90 (v/v), (3) C₂H₆/C₂H₄/CH₄/H₂/C₂H₂ (10/87/1/1/1 v/v/v/v/v) were purchased from Beijing Special Gas Co. LTD (China).

Methods

Synthesis of Fe₂(dobdc)

Anhydrous ferrous chloride (0.33g, 2.7 mmol), 2,5-dihydroxyterephthalic acid (0.213g, 1.08 mmol), anhydrous DMF (50 mL), and anhydrous methanol (6 mL) were added to a 100 mL three-neck flask in glove box filled with 99.999% N₂. The reaction mixture was heated to 393 K and stirred for 18 h to form red-orange precipitate. Methanol exchange was repeated six times during 2 days, and the solid was collected by filtration and dry in vacuum to yield Fe₂(dobdc)·solvent as a yellow-ochre powder. Fe₂(dobdc)·solvent sample was fully activated by heating under dynamic vacuum (<10⁻⁷ bar) at 433 K for 18 h and then cooled down to room temperature to yield Fe₂(dobdc) as light green powder (28). Fe₂(dobdc) is air-sensitive, so needs to be handled and stored in a dry box under N₂ atmosphere.

Synthesis of Fe₂(O₂)(dobdc)

Fe₂(O₂)(dobdc) was synthesized under carefully controlled conditions (28): About 1.3 g Fe₂(dobdc) sample was transferred into a 500 mL flask in dry glove box, then sealed and evacuated to 10⁻⁷ bar. Pure O₂ (> 99.999%) was slowly dosed to the bare Fe₂(dobdc) sample to 0.01 bar at a rate of 0.5 mbar/min under 298 K, then the O₂ pressure was brought up to 1 bar and the sample was allowed to sit for 1 h to reach equilibrium. At last, the sample was fully evacuated under high vacuum, and the free O₂ gas molecules in the pore channels were completely removed to yield Fe₂(O₂)(dobdc) as dark brown powder. Fe₂(O₂)(dobdc) is air-sensitive, so needs to be handled and stored in a dry box under N₂ atmosphere.

Sample characterization

The crystallinity and phase purity of the samples were measured using powder X-ray diffraction (PXRD) with a Rigaku Mini Flex II X-ray diffractometer employing Cu-K_α radiation operated at 30 kV and 15 mA, scanning over the range 5-40 °(2θ) at a rate of 1 %min. N₂ sorption isotherms of the samples were measured on a QUADRASORB SI at 77 K for 15 min at each point along the isotherm.

Equilibrium gas adsorption measurements

The adsorption isotherms were measured with Intelligent Gravimetric Analyser (IGA 001, Hiden, UK). Fe₂(dobdc) and Fe₂(O₂)(dobdc) samples were evacuated under 10⁻⁷ bar for 1 h before test.

Neutron diffraction experiment

Neutron powder diffraction (NPD) data were collected using the BT-1 neutron powder diffractometer at the National Institute of Standards and Technology (NIST) Center for Neutron Research. A Ge(311) monochromator with a 75 °take-off angle, $\lambda = 2.0787(2)$ Å, and in-pile collimation of 60 minutes of *arc* was used. Data were collected over the range of 1.3-166.3° (2θ) with a step size of 0.05°. Fully activated Fe₂(O₂)(dobdc) sample was loaded in a vanadium can equipped with a capillary gas line. A closed-cycle He refrigerator was used to control the sample temperature. The bare MOF sample was measured first at the temperatures 7 K. To probe the C₂H₆ and C₂H₄ adsorption locations, a pre-determined pressure (~0.5 to 1 bar) of C₂D₆ and C₂D₄ were loaded into the sample at room temperature. Diffraction data were then collected on the C₂D₆-loaded and C₂D₄-loaded Fe₂(O₂)(dobdc) samples at 7 K. (Note: deuterated gas C₂D₆/C₂D₄ was used to avoid the large incoherent neutron scattering background that would be produced by the hydrogen in C₂H₆/C₂H₄.) Rietveld structural refinement was performed on the neutron diffraction data using the GSAS package. Due to the large number of atoms in the crystal unit cell, the ligand molecule and the gas molecule were both treated as rigid bodies in the Rietveld refinement (to limit the number of variables), with the molecule orientation and center of mass freely refined. Final refinement on lattice parameters, atomic coordinates, positions/orientations of the rigid bodies, thermal factors, gas molecule occupancies, background, and profiles all converge with satisfactory R-factors.

For the bare Fe₂(O₂)(dobdc) sample, the refined O occupancy of the Fe-peroxo is close to 0.5, in good agreement with the literature value. For the gas-loaded samples, considering only one gas adsorption site (the Fe-peroxo site) was found enough to achieve good agreement in the Rietveld refinement.

Note that the structure derived from powder diffraction data refinement represents a structural average. Although all Fe atoms in the Fe₂(O₂)(dobdc) structure appear crystallographically indistinguishable, the possible existence of two chemically different Fe sites cannot be ruled out. Therefore, during the Rietveld refinement on the data of the gas-loaded samples, we also considered the possibility of gas molecules being adsorbed at two different possible locations (one directly on the presumably open-Fe site with relatively short Fe-gas distance, and the other on the Fe-peroxo site where the gas molecule is located much further from Fe). We noticed, however, data refinement always converges to a near zero occupancy of the gas molecules on the open-Fe site, strongly indicating that there are no directly C2 accessible Fe sites in the Fe₂(O₂)(dobdc) structure of our sample.

CCDC 1817715-1817716, 1574716-1574717, and 1859806-1859808 contains the supplementary crystallographic data of Fe₂(dobdc) at 298 K, and Fe₂(O₂)(dobdc),

C_2D_4 -loaded $\text{Fe}_2(\text{O}_2)(\text{dobdc})$, C_2D_6 -loaded $\text{Fe}_2(\text{O}_2)(\text{dobdc})$ at 298 K and 7 K, respectively. These data can be obtained free of charge from the Cambridge Crystallographic Data Centre via www.ccdc.cam.ac.uk/data_request/cif.

Density functional theory (DFT) calculations

DFT calculations were performed using the Quantum-Espresso package (34). A semi-empirical addition of dispersive forces to conventional DFT was included in the calculation to account for van der Waals interactions (35). We used Vanderbilt-type ultrasoft pseudopotentials and generalized gradient approximation (GGA) with a Perdew-Burke-Ernzerhof (PBE) exchange correlation. A cutoff energy of 544 eV and a $4 \times 4 \times 4$ k-point mesh (generated using the Monkhorst-Pack scheme) were found to be enough for the total energy to converge within 0.01 meV/atom. In the experimental $\text{Fe}_2(\text{O}_2)(\text{dobdc})$ structure, the O_2^{2-} occupancy on Fe is ~ 0.5 . To facilitate the calculation, $\text{Fe}_2(\text{O}_2)(\text{dobdc})$ was modeled as a simplified, fully ordered structure, where half of the Fe sites are open metal sites and the other half are bound with O_2^{2-} . The open-Fe sites and the Fe-peroxo sites are placed in an alternating arrangement with an overall crystal symmetry of $R3$, with both sites accessible to the $\text{C}_2\text{H}_4/\text{C}_2\text{H}_6$ molecules. While this model is somewhat over-simplified and at odds with our experimental finding on the inaccessibility of the open-Fe sites to $\text{C}_2\text{H}_4/\text{C}_2\text{H}_6$, it does represent a feasible platform for us to evaluate the mechanism and strength of the gas interaction with the Fe-peroxo sites. Spin-polarized calculations were performed using the primitive cell (Rhombohedral representation) of the Hexagonal crystal. We first optimized the model structure of $\text{Fe}_2(\text{O}_2)(\text{dobdc})$. We found that the ground-state magnetic configuration is antiferromagnetic, and the Fe ions are in high-spin states. C_2H_6 and C_2H_4 guest gas molecules were subsequently introduced to the Fe- O_2 sites (and the open-Fe sites for comparison) in the MOF structure, followed by full structural relaxations. The lowest-energy binding configurations were successfully obtained. To obtain the gas binding energy, an isolated gas molecule placed in a supercell (with the same cell dimensions as the $\text{Fe}_2(\text{O}_2)(\text{dobdc})$ MOF crystal) was also relaxed as a reference. The static binding energy (at $T = 0$ K) was then calculated using $E_B = E(\text{MOF}) + E(\text{gas molecule}) - E(\text{MOF} + \text{gas molecule})$.

From the calculation results, on the open-Fe site, C_2H_4 binds much stronger than C_2H_6 [in agreement with what found in $\text{Fe}_2(\text{dobdc})$], while on the Fe-peroxo site, C_2H_6 exhibits notably stronger binding than C_2H_4 , which is consistent with the experimental results. Given the fact that the experimental initial Q_{st} values of C_2H_4 and C_2H_6 in $\text{Fe}_2\text{O}_2(\text{dobdc})$ are 36.5 and 66.8 kJ/mol, respectively, the major gas adsorption sites can only be the Fe- O_2 sites. The open-Fe sites, even if there are any, shall not be accessible to $\text{C}_2\text{H}_4/\text{C}_2\text{H}_6$ molecules (although the exact reason for this inaccessibility is not clear yet). This picture is also most consistent with the structural analysis based on the NPD data.

Isosteric heat of adsorption

A Virial equation comprising of the temperature-independent parameters A_i and B_j was employed to calculate the enthalpies of adsorption for C_2H_6 and C_2H_4 in

$\text{Fe}_2(\text{O}_2)(\text{dobdc})$ and $\text{Fe}_2(\text{dobdc})$, which measured at three different temperatures 273 K, 285 K, and 298 K.

$$\ln P = \ln N + 1/T \sum_{i=0}^m a_i N_i + \sum_{j=0}^n b_j N_j \quad (1)$$

Here, P is the pressure expressed in bar, N is the amount absorbed in mmol g^{-1} , T is the temperature in K, a_i and b_j are Virial coefficients, and m , n represent the number of coefficients required to adequately describe the isotherms. The values of the Virial coefficients a_0 through a_m were then used to calculate the isosteric heat of absorption using the following expression:

$$Q_{st} = -R \sum_{i=0}^m a_i N_i \quad (2)$$

Q_{st} is the coverage-dependent isosteric heat of adsorption and R is the universal gas constant. The heat enthalpy of C_2H_6 and C_2H_4 for $\text{Fe}_2(\text{O}_2)(\text{dobdc})$ and $\text{Fe}_2(\text{dobdc})$ in this manuscript are determined by using the sorption data in the pressure range from 0-1 bar (at 273 to 298 K).

IAST calculations of adsorption selectivities and separation potential

Fitting details: The adsorption data for C_2H_6 and C_2H_4 in $\text{Fe}_2(\text{O}_2)(\text{dobdc})$ at 298 K were fitted with the 2-site Langmuir model

$$q = q_{A,sat} \frac{b_A p}{1+b_A p} + q_{B,sat} \frac{b_B p}{1+b_B p} \quad (3)$$

The 2-site Langmuir parameters for C_2H_6 , C_2H_4 , are provided in Table S2. And the corresponding isotherm fit parameters for C_2H_6 and C_2H_4 in MAF-49, ZIF-7, ZIF-8, IRMOF-8, $\text{Ni}(\text{bdc})(\text{ted})_{0.5}$, PCN-250, UTSA-33a, and UTSA-35a at 298 K are provided in Tables 3 to 10. Figure S9 to S17 presents a comparison of experimental data for C_2H_6 and C_2H_4 adsorption isotherms in all the MOFs with appropriate model fits. The fits are of good accuracy at all selected models for both guest molecules. The unary adsorption data for $\text{Ni}(\text{bdc})(\text{ted})_{0.5}$, PCN-250, UTSA-33a, and UTSA-35a are from reference 23, 24, 36, and 37, respectively.

IAST calculation: The selectivity for preferential adsorption of C_2H_6 over component C_2H_4 is defined as

$$S_{ads} = \frac{q_{C_2H_6}/q_{C_2H_4}}{y_{C_2H_6}/y_{C_2H_4}} \quad (4)$$

In equation (4) and (5), $q_{C_2H_6}$ and $q_{C_2H_4}$ are the component molar loadings of the adsorbed phase in the mixture, expressed say in the units mol kg^{-1} ; $y_{C_2H_6}$, and $y_{C_2H_4}=1-y_{C_2H_4}$, represent the mole fractions of C_2H_6 and C_2H_4 in the feed mixture.

Besides adsorption selectivities, a combined metric, called the separation potential, ΔQ , has been defined to quantify mixture separations in fixed bed adsorbents. For a $\text{C}_2\text{H}_6/\text{C}_2\text{H}_4$ mixture with mole fractions $y_{C_2H_6}$, and $y_{C_2H_4}=1-y_{C_2H_4}$, the separation potential, ΔQ , is calculated from IAST using the formula

$$\Delta Q = \left(q_{C_2H_6} \frac{y_{C_2H_4}}{1-y_{C_2H_4}} - q_{C_2H_4} \right) \rho \quad (5)$$

where ρ is the framework density. The physical significance of ΔQ , commonly expressed in the units of $\text{mmol per L of adsorbent}$, is that it represents the maximum

amount of pure C₂H₄ that can be recovered during the adsorption phase of fixed bed separations.

Transient breakthrough of mixtures in fixed bed adsorbers

For determining the productivity of polymer-grade (99.95%) C₂H₄, we performed transient breakthrough simulations using the simulation methodology described in our previous work. For the breakthrough simulations, the following parameter values were used: length of packed bed, $L = 0.3$ m; voidage of packed bed, $\varepsilon = 0.4$; superficial gas velocity at inlet, $u = 0.04$ m/s. The transient breakthrough simulation results are presented in terms of a *dimensionless* time, τ , defined by dividing the actual time, t , by the characteristic time, $L\varepsilon u^{-1}$.

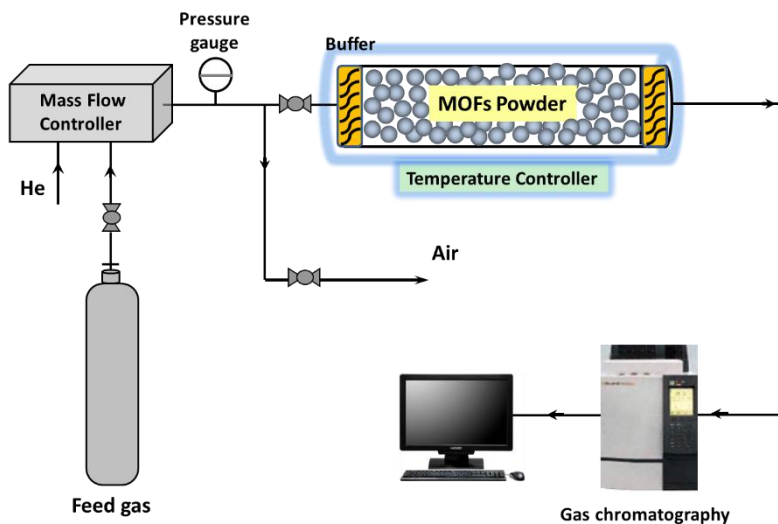
Notation

b_A	Langmuir-Freundlich constant for species i at adsorption site A, Pa ^{-ν}
b_B	Langmuir-Freundlich constant for species i at adsorption site B, Pa ^{-ν}
p_i	partial pressure of species i in mixture, Pa
p_t	total system pressure, Pa
q_i	component molar loading of species i , mol kg ⁻¹

Greek letters

ν	Freundlich exponent, dimensionless
-------	------------------------------------

Breakthrough experiment



The breakthrough experiments for C₂H₆/C₂H₄ mixtures were carried out at a flow rate of 5 mL/min (298 K, 1.01 bar). Activated MOFs powder was packed into $\phi 9 \times 150$ mm (valid column volume 3.67 cm³) stainless steel column under pure N₂ atmosphere. The experimental set-up consisted of two fixed-bed stainless steel reactors. One reactor was loaded with the adsorbent, while the other reactor was used as a blank control group to stabilize the gas flow. The horizontal reactors were placed in a temperature controlled environment, maintained at 298 K. The flow rates of all gases mixtures were regulated by mass flow controllers, and the effluent gas stream from the column is monitored by a gas chromatography (TCD-Thermal Conductivity Detector, detection limit 0.01%). Prior to the breakthrough experiment, we activated the sample by flushing the adsorption bed with helium gas for 2 h at 323 K. After every separation operation, the adsorption bed was regenerated by He flow (100 mL/min) for 1 h at 298 K.

The C₂H₄ productivity (q) is defined by the breakthrough amount of C₂H₄, which is calculated by integration of the breakthrough curves $f(t)$ during a period from t_1 to t_2 where the C₂H₄ purity is higher than or equal to a threshold value p :

$$q = \frac{c_i(C_2H_4)}{c_i(C_2H_4) + c_i(C_2H_6)} \times (\int_{t_1}^{t_2} f(t) dt) \quad (6)$$

Tables S1 to S15

Table S1. DFT-D calculated static gas binding energies (unit: kJ/mol) on the two potential adsorption sites in the simplified structural model of Fe₂(O₂)(dobdc).

	Fe-peroxo site	Open-Fe site
C ₂ H ₄	35.9	58.2
C ₂ H ₆	46.5	27.2

Table S2. 2-site Langmuir fitting parameters for C₂H₄ and C₂H₆ in Fe₂(O₂)(dobdc).

	Site A		Site B	
	$q_{A,\text{sat}}$ mmol g ⁻¹	b_A Pa ⁻¹	$q_{B,\text{sat}}$ mmol g ⁻¹	b_B Pa ⁻¹
C ₂ H ₄	2.813	4.711E-4	3.017	7.742E-7
C ₂ H ₆	3.399	1.48E-4	1.302	1.46E-7

Table S3. 2-site Langmuir-Freundlich fitting parameters for C₂H₄ and C₂H₆ in MAF-49.

	Site A			Site B		
	$q_{A,\text{sat}}$ mmol g ⁻¹	b_A Pa ^{-ν_f}	$ν_A$ dimensionless	$q_{B,\text{sat}}$ mmol g ⁻¹	b_B Pa ^{-ν_f}	$ν_B$ dimensionless
C ₂ H ₄	0.402	1.13E-4	2.403	1.304	2.63E-5	1.608
C ₂ H ₆	1.719	8.37E-3	0.998			

Table S4. 2-site Langmuir-Freundlich fitting parameters for C₂H₄ and C₂H₆ in ZIF-7.

	Site A			Site B		
	$q_{A,\text{sat}}$ mmol g ⁻¹	b_A Pa ^{-ν_i}	$ν_A$ dimensionless	$q_{B,\text{sat}}$ mmol g ⁻¹	b_B Pa ^{-ν_i}	$ν_B$ dimensionless
C ₂ H ₄	1.727	4.4E-27	5.703	0.098	4E-5	1.024
C ₂ H ₆	1.905	4.36E-15	3.196	0.011	0.03	0.997

Table S5. 1-site Langmuir fitting parameters for C₂H₄ and C₂H₆ in ZIF-8.

	$q_{A,\text{sat}}$ (mmol g ⁻¹)	b_A (Pa ⁻¹)
C ₂ H ₄	4.308	3.59E-6
C ₂ H ₆	6.122	3.84E-6

Table S6. 1-site Langmuir-Freundlich fitting parameters for C₂H₄ and C₂H₆ in IRMOF-8.

	$q_{A,\text{sat}}$ mmol g ⁻¹	b_A Pa ^{-ν_i}	$ν_A$ dimensionless
C ₂ H ₄	11.203	1.21E-4	0.76
C ₂ H ₆	6.201	2.51E-4	0.83

Table S7. 2-site Langmuir-Freundlich fitting parameters for C₂H₄ and C₂H₆ in Ni(bdc)(ted)_{0.5}.

	Site A			Site B		
	$q_{A,\text{sat}}$ mmol g ⁻¹	b_A Pa ^{-ν_i}	$ν_A$ dimensionless	$q_{B,\text{sat}}$ mmol g ⁻¹	b_B Pa ^{-ν_i}	$ν_B$ dimensionless
C ₂ H ₄	38.286	1.925E-7	1.069	6.363	6.61E-7	1.138
C ₂ H ₆	7.761	9.89E-8	1.4	2.99	8.4E-6	0.974

Table S8. 2-site Langmuir-Freundlich fitting parameters for C₂H₄ and C₂H₆ in PCN-250.

	Site A			Site B		
	$q_{A,\text{sat}}$ mmol g ⁻¹	b_A Pa ^{-ν_i}	$ν_A$ dimensionless	$q_{B,\text{sat}}$ mmol g ⁻¹	b_B Pa ^{-ν_i}	$ν_B$ dimensionless
C ₂ H ₄	8.002	4.29E-5	0.805	1.441	1.81E-5	0.688
C ₂ H ₆	14.002	7.33E-5	0.6	4.82	1.56E-6	1.34

Table S9. 2-site Langmuir fitting parameters for C₂H₄ and C₂H₆ in UTSA-33a.

	Site A		Site B	
	$q_{A,\text{sat}}$ mmol g ⁻¹	b_A Pa ^{-ν_i}	$q_{B,\text{sat}}$ mmol g ⁻¹	b_B Pa ^{-ν_i}
C ₂ H ₄	3.702	2.13E-5	4.704	3.86E-7
C ₂ H ₆	3.106	4.03E-5	1.611	1.787E-6

Table S10. 2-site Langmuir fitting parameters for C₂H₄ and C₂H₆ in UTSA-35a.

	Site A		Site B	
	$q_{A,\text{sat}}$ mmol g ⁻¹	b_A Pa ⁻¹	$q_{B,\text{sat}}$ mmol g ⁻¹	b_B Pa ⁻¹
C ₂ H ₄	4.013	7.27E-6	0.505	5.31E-5
C ₂ H ₆	3.65	1.66E-5	0.098	1.78E-4

Table S11. Comparison of the adsorption selectivities of the selected MOFs for C₂H₆/C₂H₄ (50/50) at 298 K and 1 bar, calculated by IAST method.

	This work	Literature reported values	References
Fe ₂ (O ₂)(dobdc)	4.4	/	/
ZIF-8	1.7	2.0	<i>Chem. Eng. Sci.</i> , 2015 , 124, 144-153.
ZIF-7	1.6	2.2	<i>Micropor. Mesopor. Mater.</i> , 2015 , 208, 55-65.
MAF-49	2.7	/	/
IRMOF-8	1.8	1.6	<i>ACS Appl. Mater. Inter.</i> , 2014 , 6, 12093-12099.
UTSA-33a	1.4	/	/
UTSA-35a	1.4	/	/
PCN-250	1.9	1.9	<i>Chem. Eng. Sci.</i> , 2018 , 175, 110-117.
Ni(bdc)(ted) _{0.5}	1.6	/	/

Table S12. Breakthrough calculations for separation of C₂H₆/C₂H₄ mixture (50/50 v/v) at 298 K. The product gas stream contains more than 99.95% C₂H₄.

	Separation potential ΔQ	99.95% pure C ₂ H ₄ recovered
	mmol L ⁻¹	mmol L ⁻¹
Fe ₂ (O ₂)(dobdc)	2183	2172
ZIF-8	334	95
ZIF-7	429	36
MAF-49	1157	766
IRMOF-8	645	313
UTSA-33a	428	1
UTSA-35a	0	0
PCN-250	1758	894
Ni(bdc)(ted) _{0.5}	0	0

Table S13. Breakthrough calculations for separation of C₂H₆/C₂H₄ mixture (10/90 v/v) at 298 K. The product gas stream contains less than 0.05% C₂H₆.

	Separation potential ΔQ	99.95% pure C ₂ H ₄ recovered
	mmol L ⁻¹	mmol L ⁻¹
Fe ₂ (O ₂)(dobdc)	6855	6333
ZIF-8	607	231
ZIF-7	883	68
MAF-49	3306	1833
IRMOF-8	1654	766
UTSA-33a	892	148
UTSA-35a	788	128
PCN-250	3766	1811
Ni(bdc)(ted) _{0.5}	1547	513

Table S14. Comparisons of the breakthrough columns parameters studied in this work.

	Sample weight (g)	Crystal density (g/cm ³)	Packing density (g/cm ³)	Column voidage	Column free space (cm ³)
Fe ₂ (O ₂)(dobdc)	3.372	1.255	0.919	0.268	0.983
MAF-49	3.984	1.481	1.086	0.267	0.979
ZIF-7	3.314	1.241	0.903	0.272	0.998
ZIF-8	2.929	1.067	0.798	0.252	0.924
IRMOF-8	2.374	0.896	0.647	0.276	1.012
PCN-250	2.635	0.957	0.718	0.249	0.914

Packing density = Sample weight / Column volume (The valid column volume in this work is 3.67 cm³)

Column voidage = 1 - Sample weight / Crystal density / Column volume

Column free space = Column volume × Column voidage

Table S15. Comparisons of C₂H₄ productivities of selected MOFs in experimental breakthrough operation using C₂H₆/C₂H₄ mixture (50/50 v/v) as input.

Gravimetric Productivity (mmol g ⁻¹) with different purities of C ₂ H ₄						
	This work			Literature reported values (2, 24)		
	99.99%+	99.95%+	99%+	99.99%+	99.95%+	99%+
Fe ₂ (O ₂)(dobdc)	0.79	0.83	0.89	/	/	/
MAF-49	0.28	0.31	0.32	/	0.28	0.32
ZIF-7	0	0	0.01	0	0	0.01
ZIF-8	0	0	0.03	0	0	0.03
IRMOF-8	0	0	0.12	0	0	0.11
PCN-250	0	0.03	0.05	0	0	0.15

Figs. S1 to S20

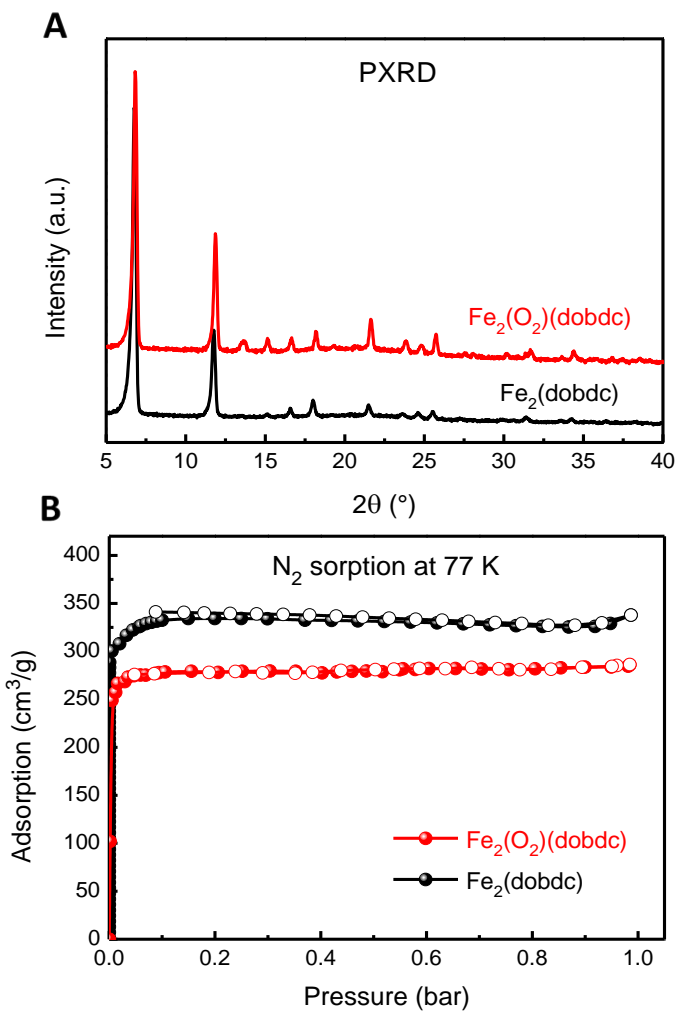


Fig. S1.

(A) Powder X-ray diffraction (PXRD) patterns of $\text{Fe}_2(\text{dobdc})$ and $\text{Fe}_2(\text{O}_2)(\text{dobdc})$, which confirm that $\text{Fe}_2(\text{O}_2)(\text{dobdc})$ maintains the framework structure of $\text{Fe}_2(\text{dobdc})$. (B) N_2 -sorption data for $\text{Fe}_2(\text{dobdc})$ and $\text{Fe}_2(\text{O}_2)(\text{dobdc})$ measured at 77 K. The BET (Brunauer-Emmett-Teller) surface area of $\text{Fe}_2(\text{O}_2)(\text{dobdc})$ is $1073 \text{ m}^2/\text{g}$, slightly lower than that of $\text{Fe}_2(\text{dobdc})$ ($1292 \text{ m}^2/\text{g}$), as expected.

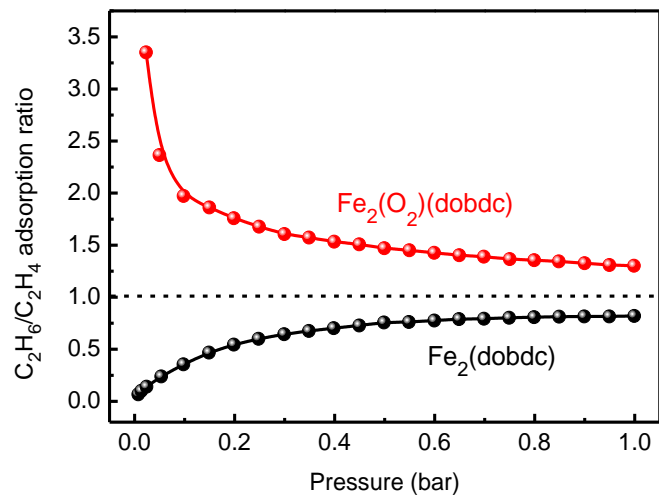


Fig. S2.

C₂H₆/C₂H₄ adsorption ratios for Fe₂(O₂)(dobdc) (red) and Fe₂(dobdc) (black), calculated from their single-component adsorption isotherms at 298 K.

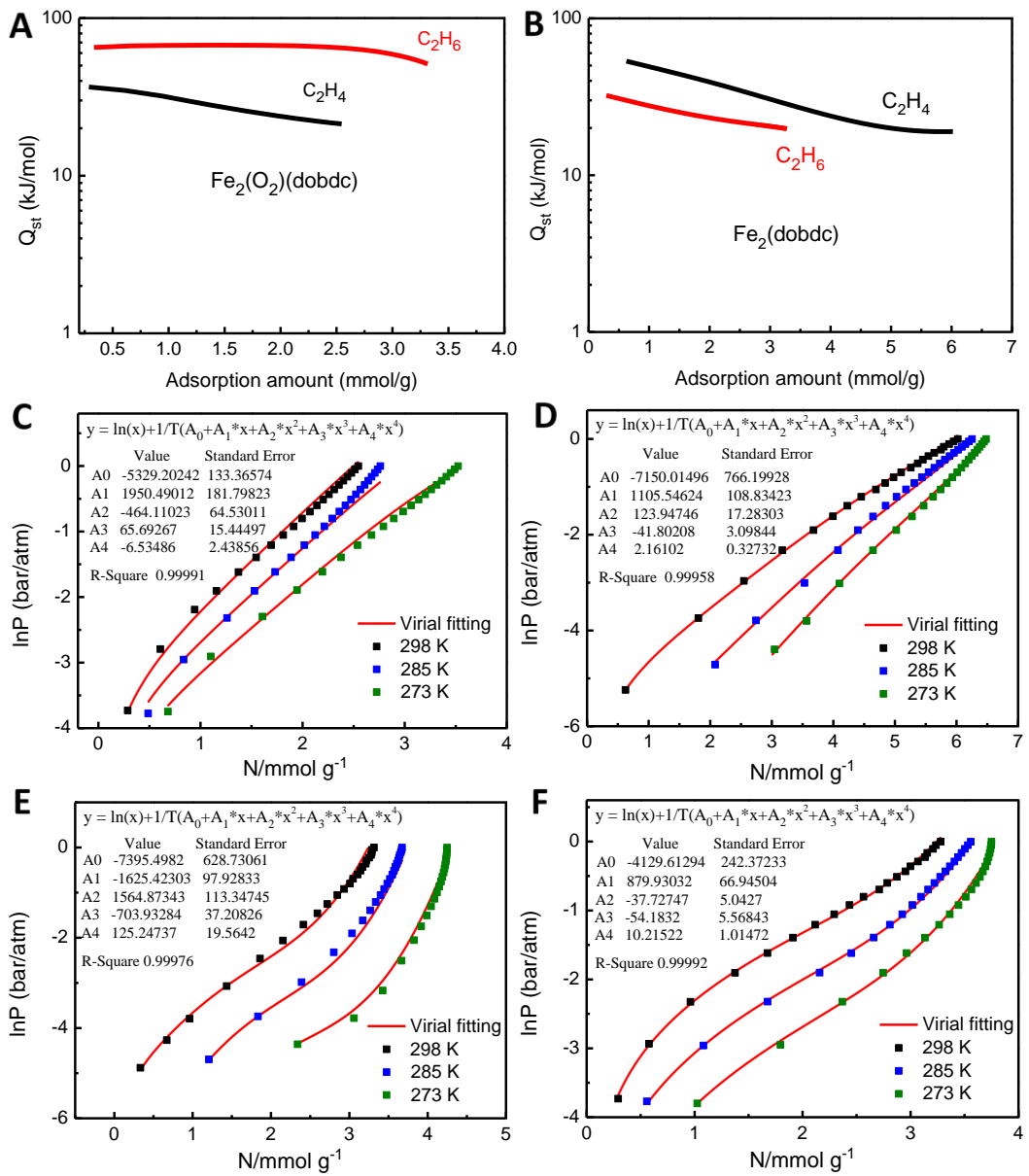


Fig. S3.

Adsorption heats and the corresponding virial fitting of the C_2H_6 and C_2H_4 adsorption isotherms (points) of $\text{Fe}_2(\text{O}_2)\text{(dobdc)}$ (C: C_2H_4 , E: C_2H_6) and $\text{Fe}_2\text{(dobdc)}$ (D: C_2H_4 , F: C_2H_6) at 298 K (black), 285 K (blue), and 273 K (Green).

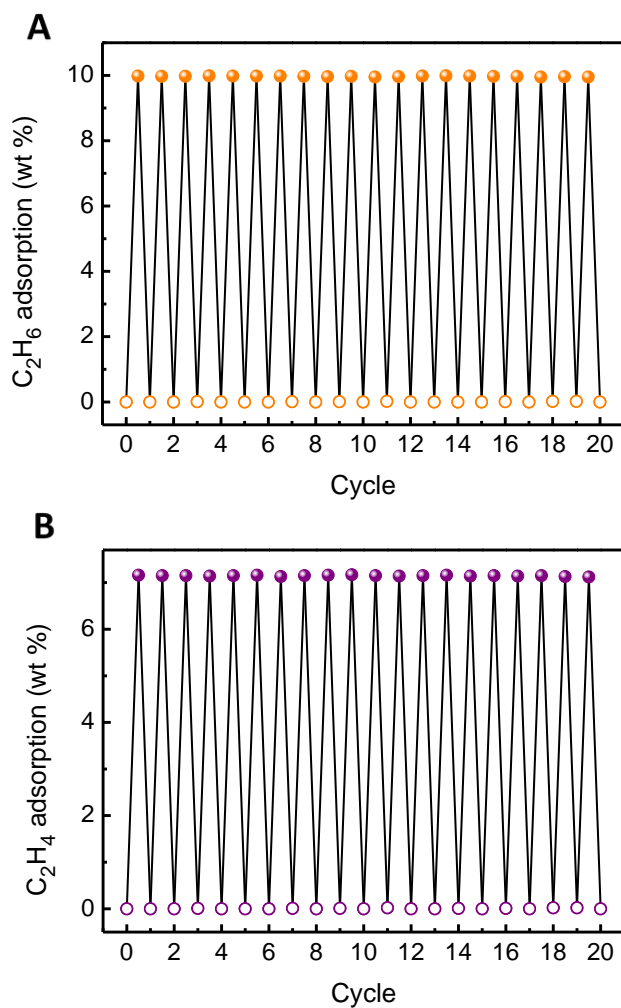


Fig. S4.

(A) C_2H_6 and (B) C_2H_4 adsorption cycling in $\text{Fe}_2(\text{O}_2)(\text{dobdc})$. Adsorption (solid circles): pure gas at 298 K and 1 bar; Desorption (empty circles): under dynamic vacuum (10^{-7} bar) at 298 K for 1 hour.

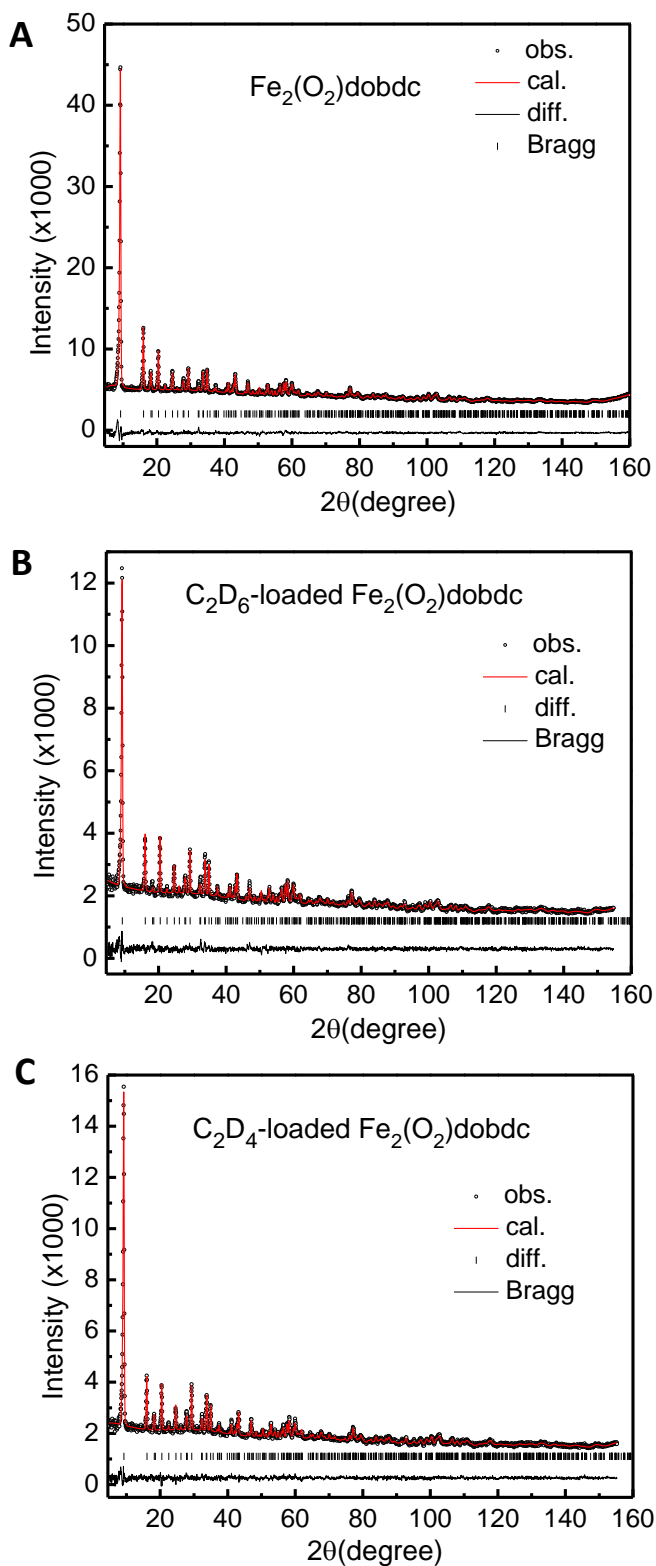


Fig. S5.

Rietveld refinements of the neutron powder diffraction data for (A) bare $\text{Fe}_2(\text{O}_2)\text{dobdc}$, (B) C_2D_6 - and (C) C_2D_4 -loaded $\text{Fe}_2(\text{O}_2)\text{dobdc}$ measured at 7 K. Goodness of fit parameters of the refinements: (A) $R_p=0.0202$, $R_{wp}=0.0163$, $\chi^2=1.33$; (B) $R_p=0.0223$, $R_{wp}=0.0198$, $\chi^2=0.98$; (C) $R_p=0.0235$, $R_{wp}=0.0196$, $\chi^2=1.01$.

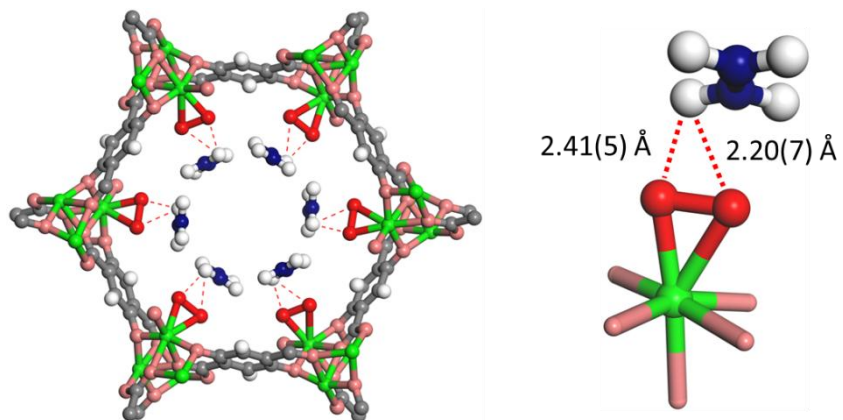


Fig. S6.

Crystal structure of $\text{Fe}_2(\text{O}_2)(\text{dobdc}) \cdot \text{C}_2\text{D}_4$ from neutron diffraction at 7 K. (Fe, green; C, dark grey; O, pink; O_2^{2-} , red; H or D, white; C in C_2D_4 , blue).

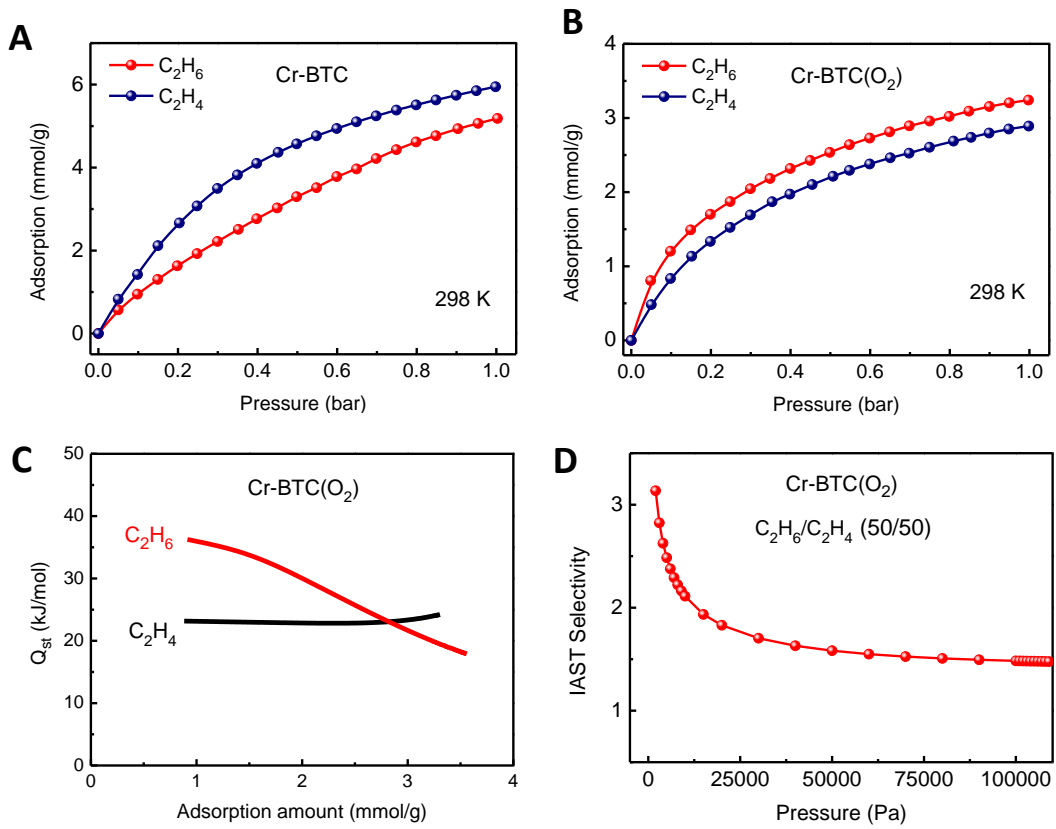


Fig. S7.

(A and B) C_2H_6 and C_2H_4 adsorption isotherms of Cr-BTC and Cr-BTC(O_2) at 298 K. (C) Adsorption heats for C_2H_6 and C_2H_4 in Cr-BTC(O_2), calculated by using the Virial equation. (D) IAST selectivity of Cr-BTC(O_2) for C_2H_6/C_2H_4 at 298 K. Cr-BTC and Cr-BTC(O_2) were synthesized according to the procedure in reference 30.

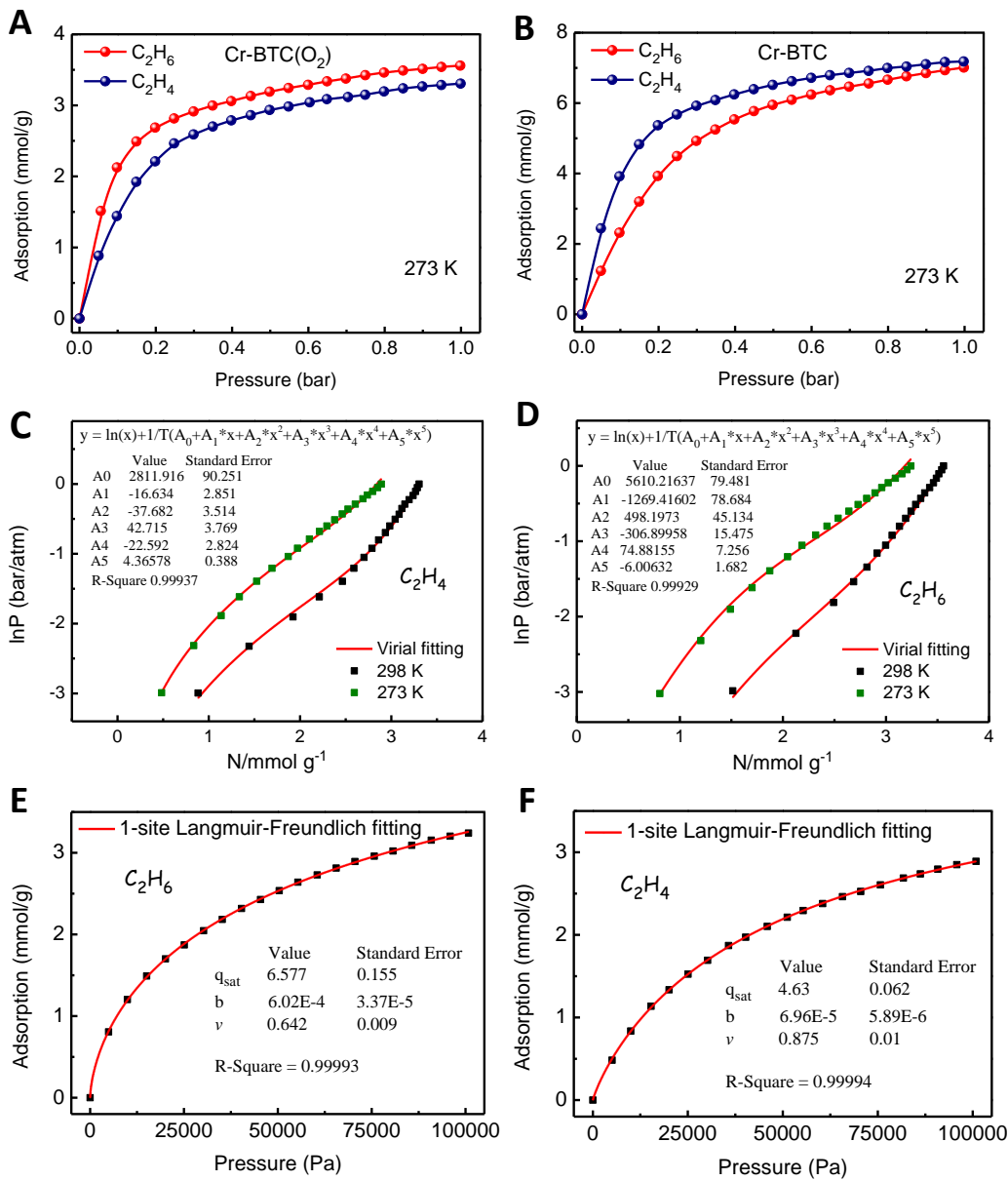


Fig. S8.

(A and B) C_2H_6 and C_2H_4 adsorption isotherms of Cr-BTC and $\text{Cr-BTC}(\text{O}_2)$ at 273 K. (C and D) Virial fitting of the C_2H_6 and C_2H_4 adsorption isotherms (points) of $\text{Cr-BTC}(\text{O}_2)$ measured at 298 K. (E and F) 1-site Langmuir-Freundlich fitting (lines) of C_2H_6 and C_2H_4 adsorption isotherms (points) of $\text{Cr-BTC}(\text{O}_2)$ measured at 298 K.

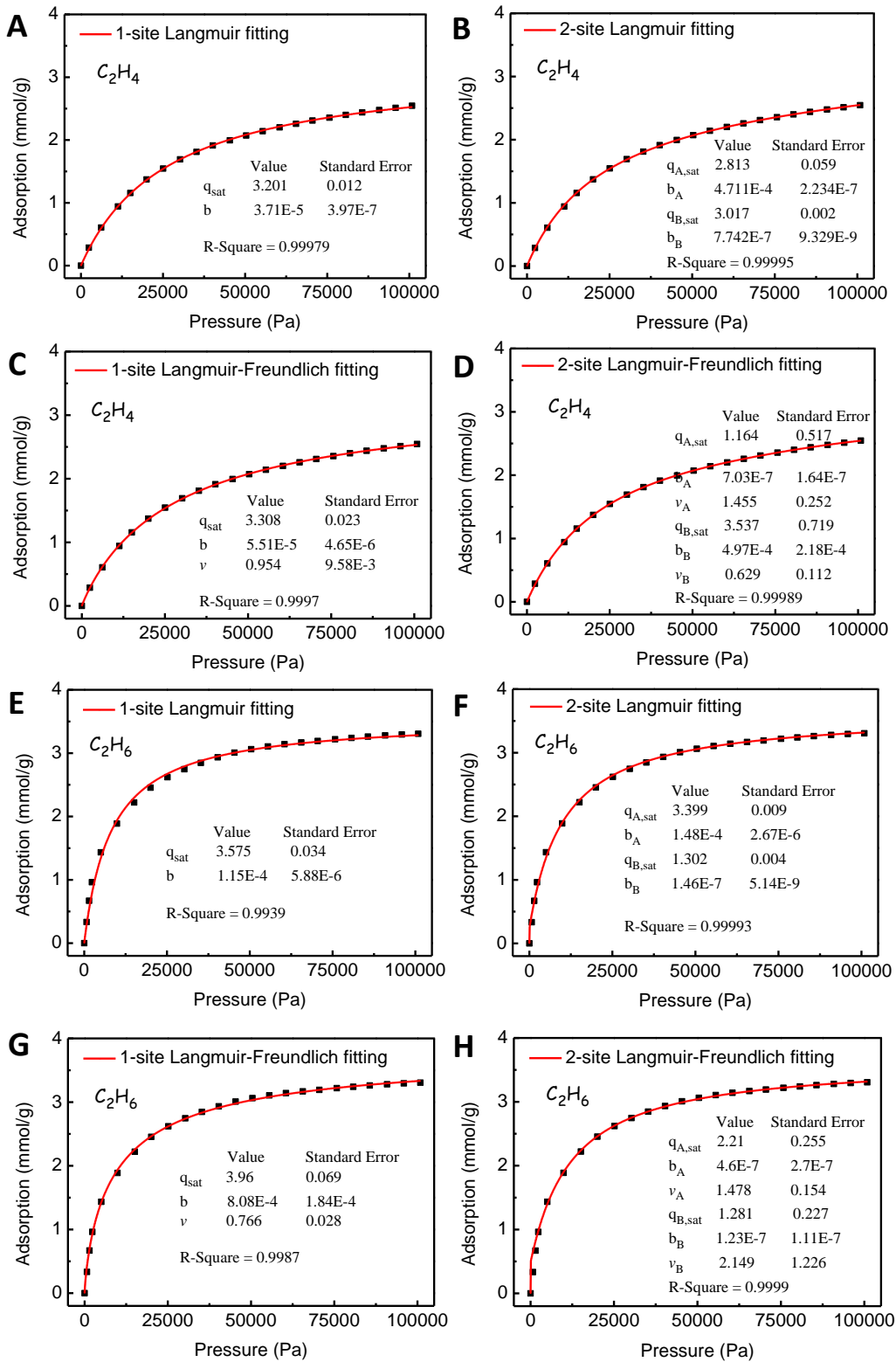


Fig. S9.

1-site Langmuir fitting, 2-site Langmuir fitting, 1-site Langmuir-Freundlich fitting, and 2-site Langmuir-Freundlich fitting (lines) of the (A-D) C_2H_4 and (E-H) C_2H_6 adsorption isotherms (points) of $Fe_2(O_2)dobdc$ at 298 K. It can be seen that 2-site Langmuir fittings for both gases molecule have the highest R -Square values (B and F) and acceptable standard error.

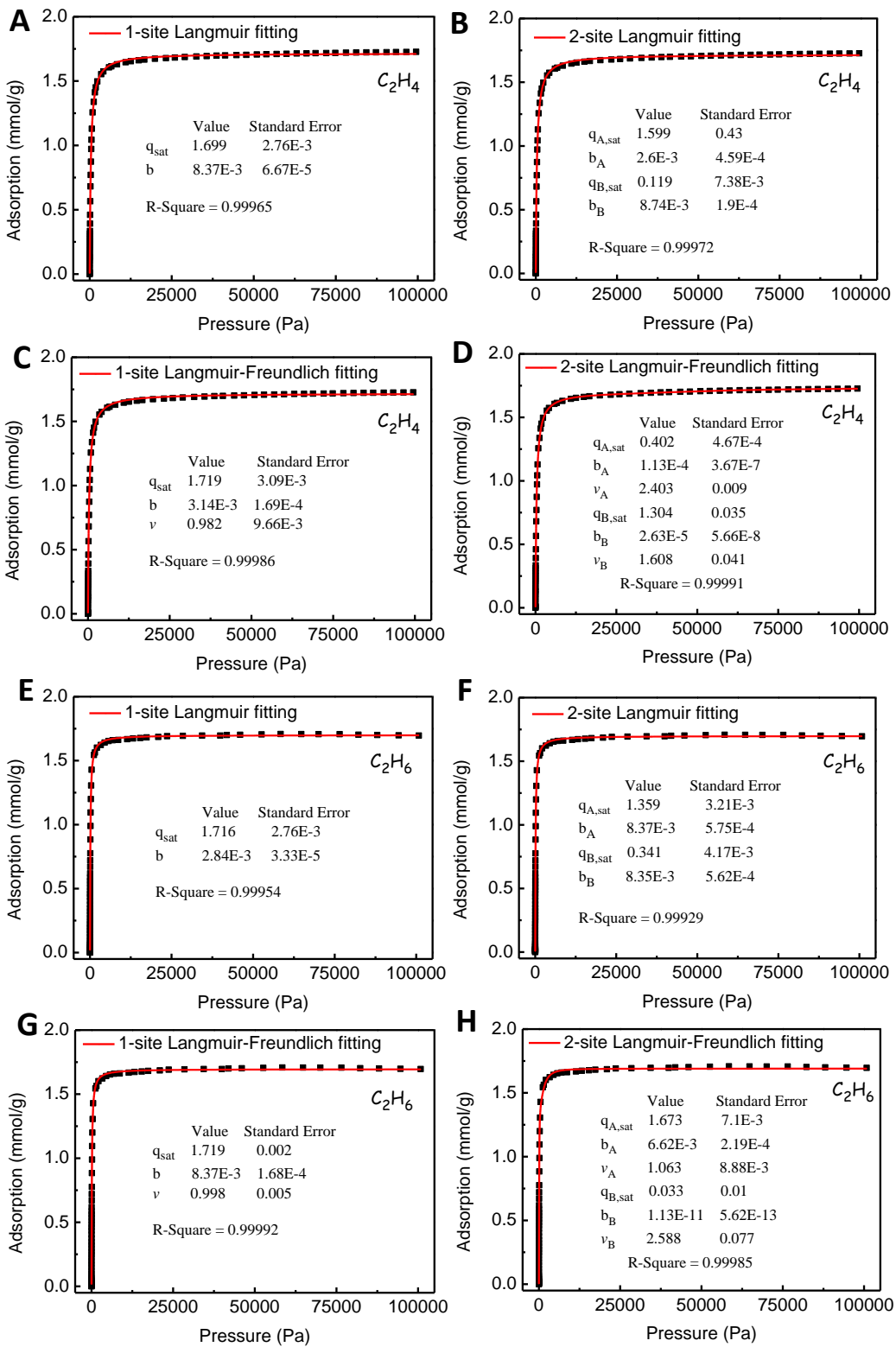


Fig. S10.

1-site Langmuir fitting, 2-site Langmuir fitting, 1-site Langmuir-Freundlich fitting, and 2-site Langmuir-Freundlich fitting (lines) of the (A-D) C_2H_4 and (E-H) C_2H_6 adsorption isotherms (points) of MAF-49 at 298 K. It can be seen that 2-site Langmuir-Freundlich for C_2H_4 (D) and 1-site Langmuir-Freundlich fitting for C_2H_6 (G) have the highest R-Square values and acceptable standard error.

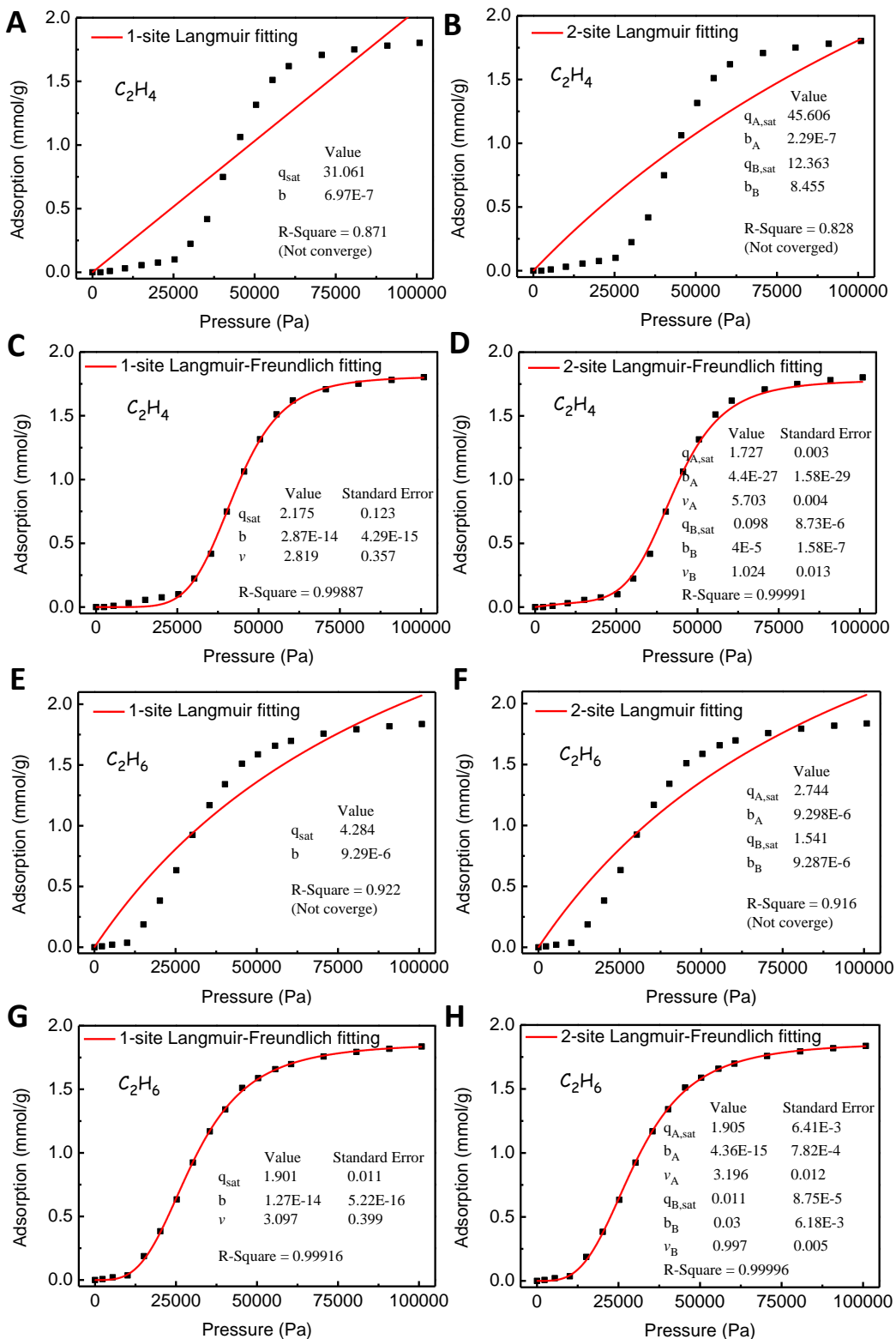


Fig. S11.

1-site Langmuir fitting, 2-site Langmuir fitting, 1-site Langmuir-Freundlich fitting, and 2-site Langmuir-Freundlich fitting (lines) of the (A-D) C_2H_4 and (E-H) C_2H_6 adsorption isotherms (points) of ZIF-7 at 298 K. It can be seen that 2-site Langmuir-Freundlich fittings for both gases molecule have the highest R-Square values (D and H) and acceptable standard error.

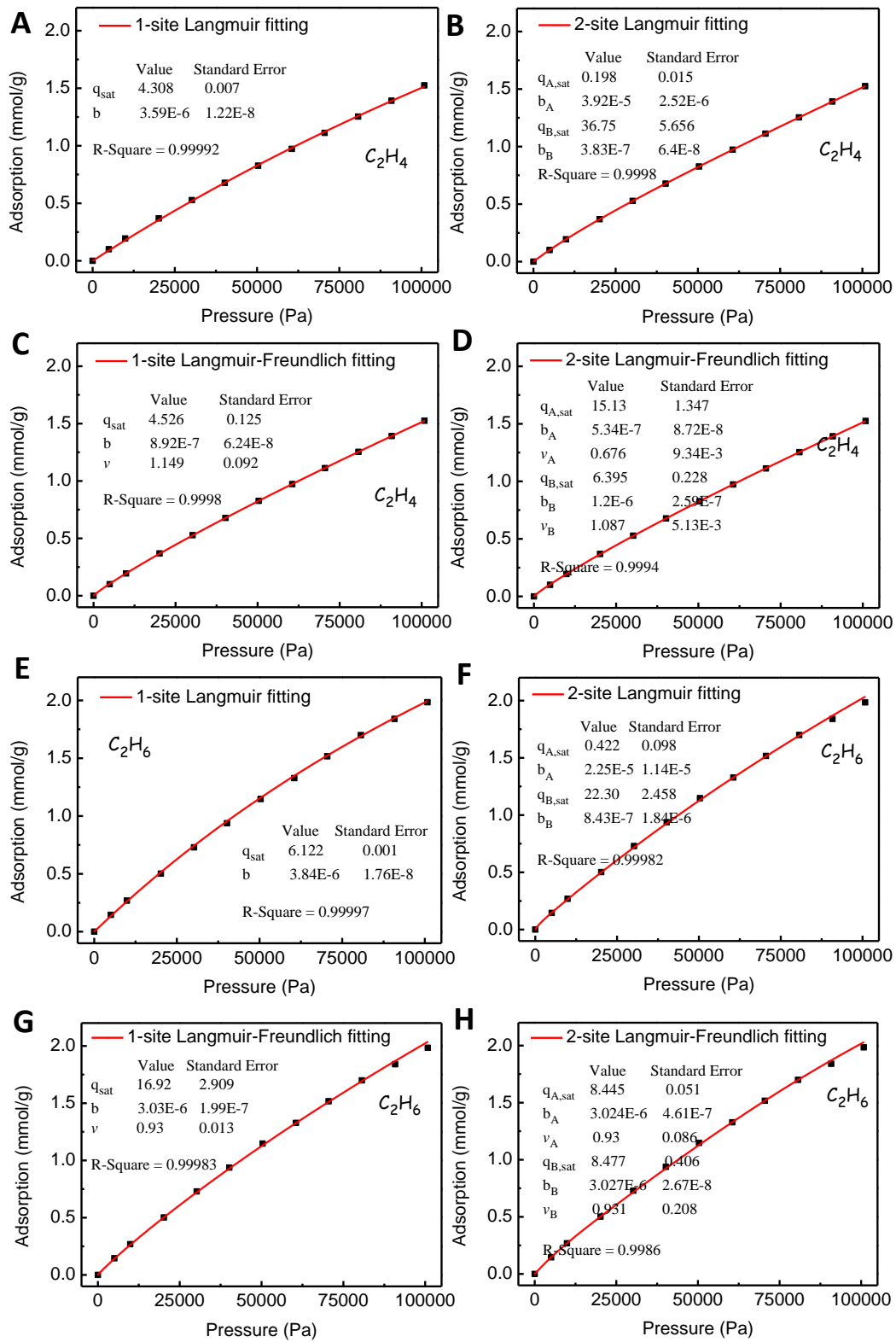


Fig. S12.

1-site Langmuir fitting, 2-site Langmuir fitting, 1-site Langmuir-Freudlich fitting, and 2-site Langmuir-Freudlich fitting (lines) of the (A-D) C_2H_4 and (E-H) C_2H_6 adsorption isotherms (points) of ZIF-8 at 298 K. It can be seen that 1-site Langmuir fittings for both gases molecule have the highest R-Square values (A and E) and acceptable standard error.

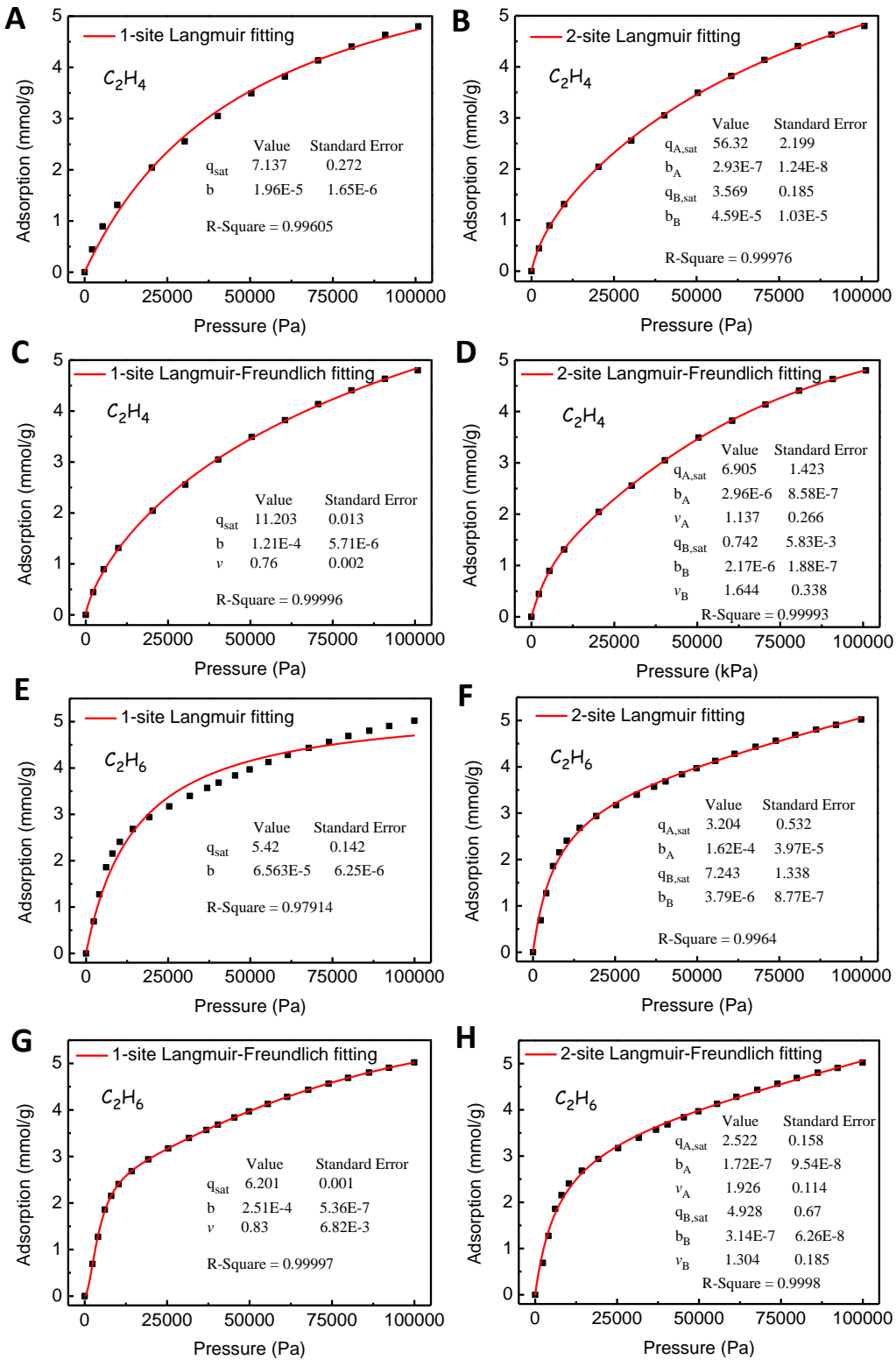


Fig. S13.

1-site Langmuir fitting, 2-site Langmuir fitting, 1-site Langmuir-Freudlich fitting, and 2-site Langmuir-Freudlich fitting (lines) of the (A-D) C_2H_4 and (E-H) C_2H_6 adsorption isotherms (points) of IRMOF-8 at 298 K. It can be seen that 1-site Langmuir-Freudlich fittings for both gases molecule have the highest *R*-Square values (C and G) and acceptable standard error.

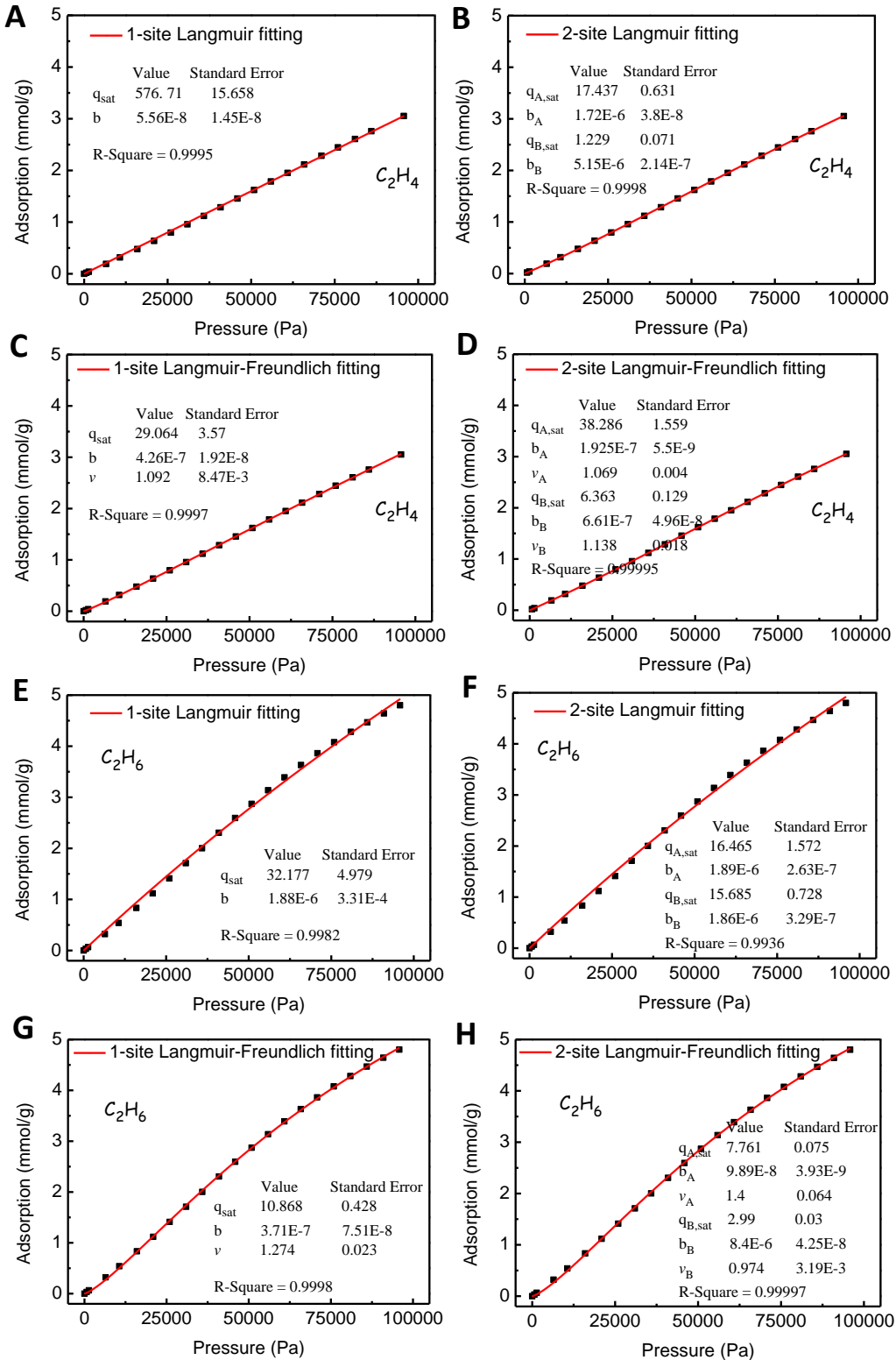


Fig. S14.

1-site Langmuir fitting, 2-site Langmuir fitting, 1-site Langmuir-Freundlich fitting, and 2-site Langmuir-Freundlich fitting (lines) of the (A-D) C_2H_4 and (E-H) C_2H_6 adsorption isotherms (points) of $\text{Ni}(\text{bdc})(\text{ted})_{0.5}$ at 298 K. It can be seen that 2-site Langmuir-Freundlich fittings for both gases molecule have the highest R-Square values (D and H) and acceptable standard error.

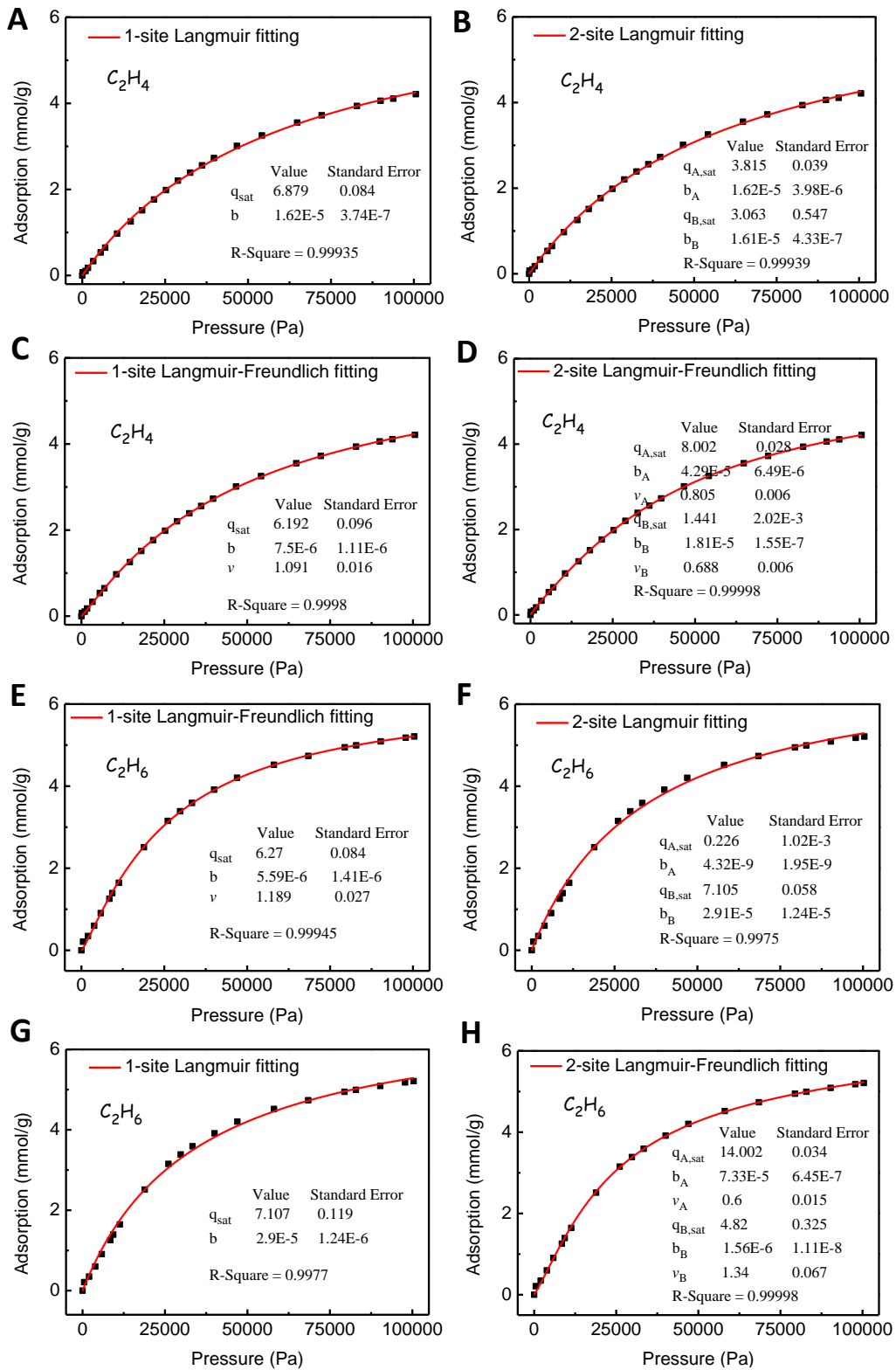


Fig. S15.

1-site Langmuir fitting, 2-site Langmuir fitting, 1-site Langmuir-Freundlich fitting, and 2-site Langmuir-Freundlich fitting (lines) of the (A-D) C_2H_4 and (E-H) C_2H_6 adsorption isotherms (points) of PCN-250 at 298 K. It can be seen that 2-site Langmuir-Freundlich fittings for both gases molecule have the highest *R*-Square

values (D and H) and acceptable standard error.

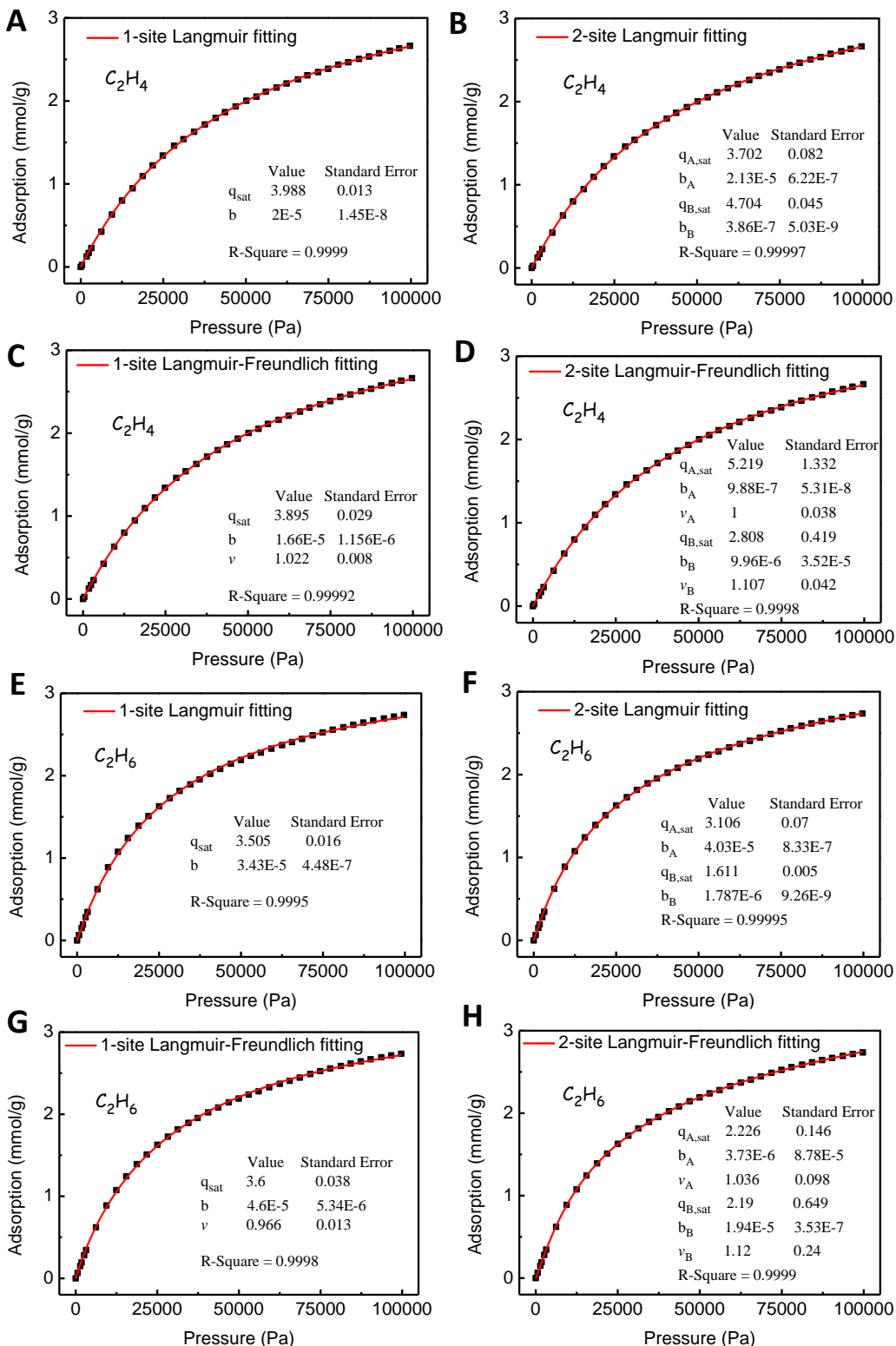


Fig. S16.

1-site Langmuir fitting, 2-site Langmuir fitting, 1-site Langmuir-Freundlich fitting, and 2-site Langmuir-Freundlich fitting (lines) of the (A-D) C_2H_4 and (E-H) C_2H_6 adsorption isotherms (points) of UTSA-33a at 298 K. It can be seen that 2-site Langmuir fittings for both gases molecule have the highest R-Square values (B and F)

and acceptable standard error.

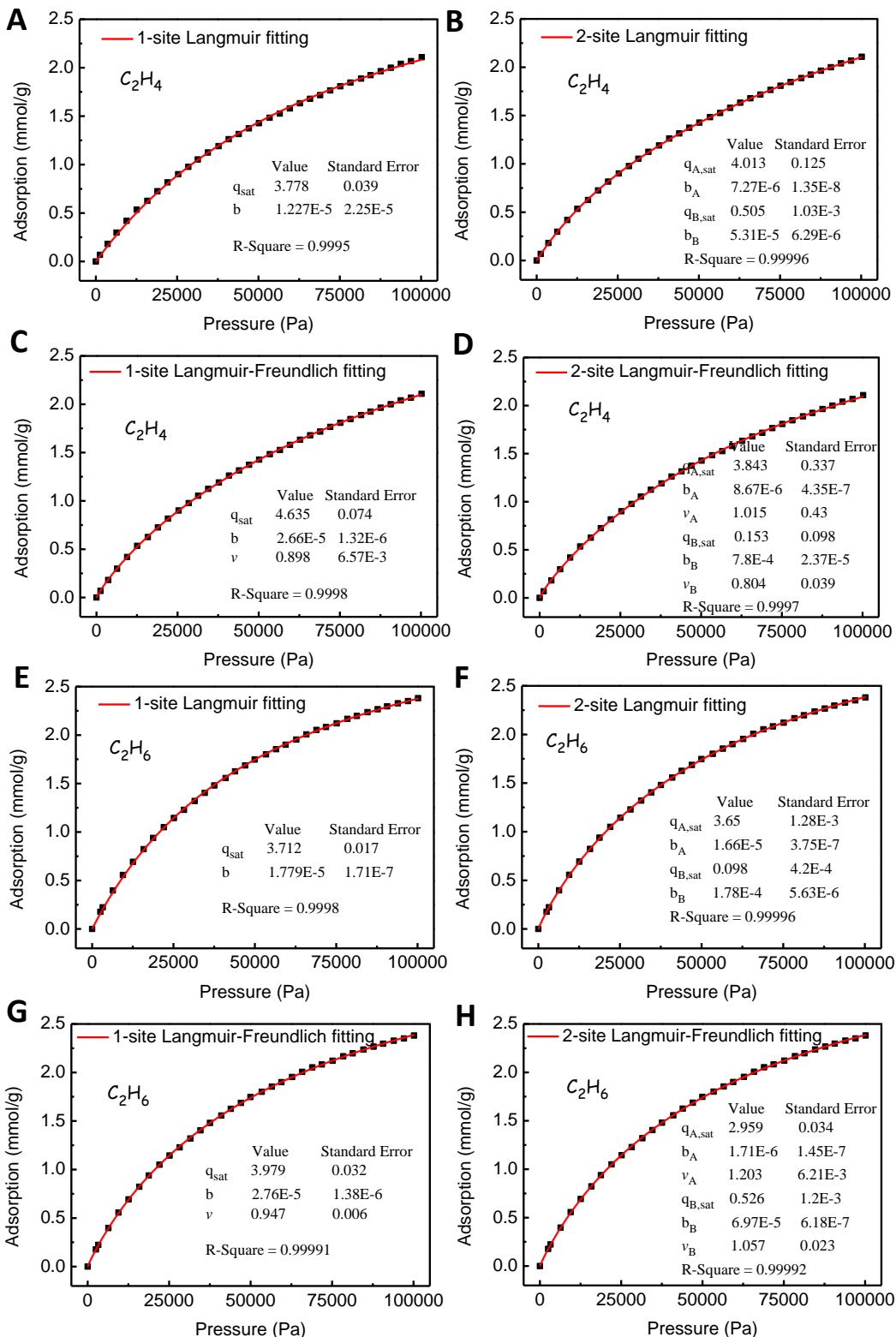


Fig. S17.

1-site Langmuir fitting, 2-site Langmuir fitting, 1-site Langmuir-Freundlich fitting, and 2-site Langmuir-Freundlich fitting (lines) of the (A-D) C_2H_4 and (E-H) C_2H_6 adsorption isotherms (points) of UTSA-35a at 298 K. It can be seen that 2-site Langmuir fittings for both gases molecule have the highest $R\text{-}Square$ values (B and F)

and acceptable standard error.

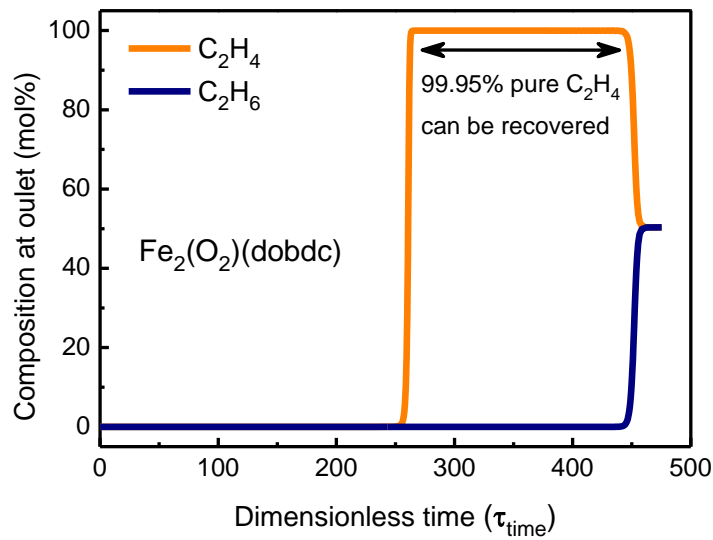


Fig. S18.

Transient breakthrough curves for $\text{C}_2\text{H}_6/\text{C}_2\text{H}_4$ (50/50) mixture in a fixed bed packed with $\text{Fe}_2(\text{O}_2)(\text{dobdc})$ at 298 K. The normalized gas phase molar concentrations of C_2H_6 , and C_2H_4 exiting the fixed bed adsorber are plotted against the dimensionless time, τ .

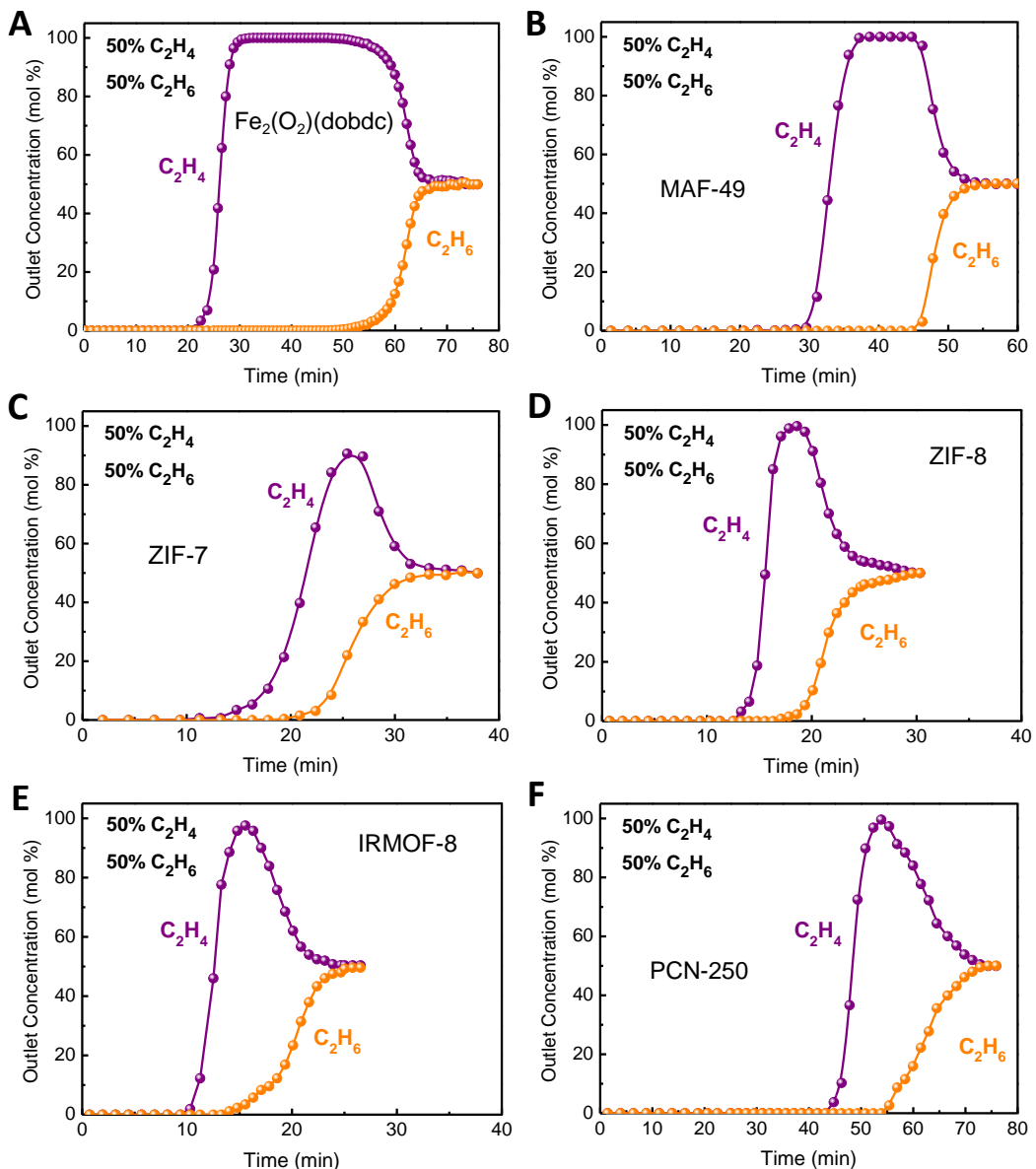


Fig. S19.

Breakthrough curves of (A) $\text{Fe}_2(\text{O}_2)(\text{dobdc})$, (B) MAF-49, (C) ZIF-7, (D) ZIF-8, (E) IRMOF-8, (F) $\text{Ni}(\text{bdc})(\text{ted})_{0.5}$, and (G) PCN-250 for $\text{C}_2\text{H}_4/\text{C}_2\text{H}_6$ (50:50) mixture, measured at 298 K and 1.01 bar.

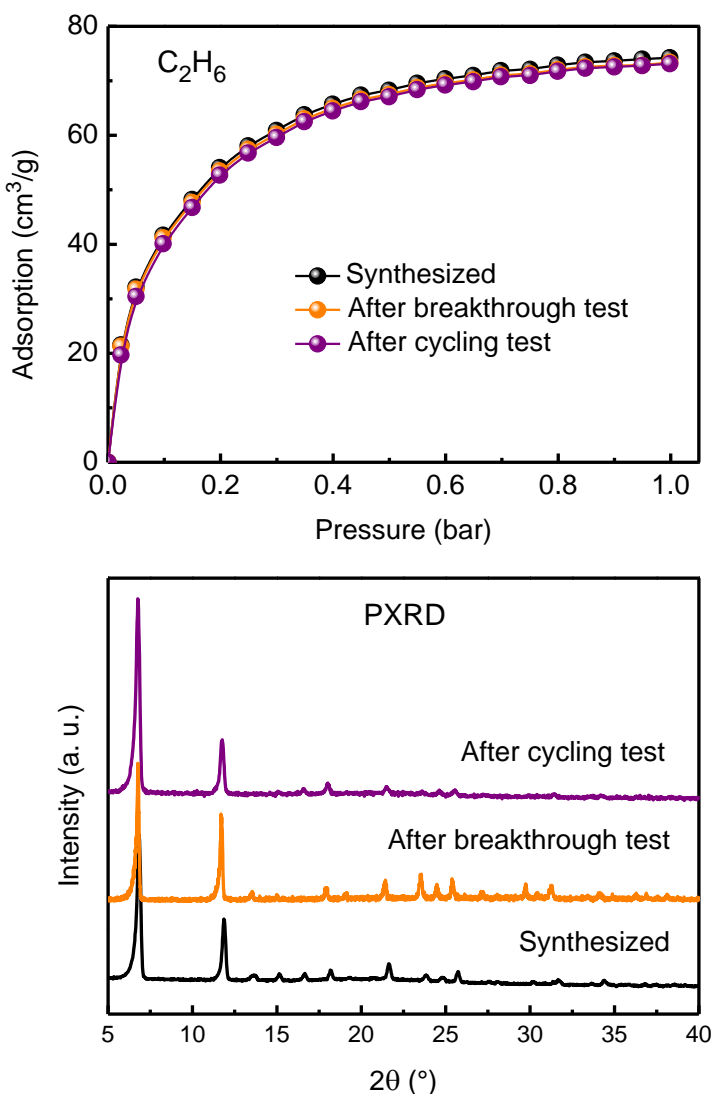


Fig. S20.

C_2H_6 adsorption isotherms (298 K) and PXRD patterns of $\text{Fe}_2(\text{O}_2)(\text{dobdc})$ after breakthrough and cycling tests.

Disclaimer: Certain commercial suppliers are identified in this paper to foster understanding. Such identification does not imply recommendation or endorsement by the National Institute of Standards and Technology, nor does it imply that the materials or equipment identified are necessarily the best available for the purpose.

References and Notes

1. F. Bander, Separation Technologies; <http://seperationtechnology.com>.
2. P.-Q. Liao, W.-X. Zhang, J.-P. Zhang, X.-M. Chen, Efficient purification of ethene by an ethane-trapping metal-organic framework. *Nat. Commun.* **6**, 8697 (2015).
[doi:10.1038/ncomms9697](https://doi.org/10.1038/ncomms9697) [Medline](#)
3. D. S. Sholl, R. P. Lively, Seven chemical separations to change the world. *Nature* **532**, 435–437 (2016). [doi:10.1038/532435a](https://doi.org/10.1038/532435a) [Medline](#)
4. J. Y. S. Lin, Molecular sieves for gas separation. *Science* **353**, 121–122 (2016).
[doi:10.1126/science.aag2267](https://doi.org/10.1126/science.aag2267) [Medline](#)
5. S. Chu, Y. Cui, N. Liu, The path towards sustainable energy. *Nat. Mater.* **16**, 16–22 (2016).
[doi:10.1038/nmat4834](https://doi.org/10.1038/nmat4834) [Medline](#)
6. R. T. Yang, E. S. Kikkinides, New sorbents for olefin/paraffin separations by adsorption via π -complexation. *AIChE J.* **41**, 509–517 (1995). [doi:10.1002/aic.690410309](https://doi.org/10.1002/aic.690410309)
7. P. J. Bereciartua, Á. Cantín, A. Corma, J. L. Jordá, M. Palomino, F. Rey, S. Valencia, E. W. Corcoran Jr., P. Kortunov, P. I. Ravikovich, A. Burton, C. Yoon, Y. Wang, C. Paur, J. Guzman, A. R. Bishop, G. L. Casty, Control of zeolite framework flexibility and pore topology for separation of ethane and ethylene. *Science* **358**, 1068–1071 (2017).
[doi:10.1126/science.aoa0092](https://doi.org/10.1126/science.aoa0092) [Medline](#)
8. S. Aguado, G. Bergeret, C. Daniel, D. Farrusseng, Absolute molecular sieve separation of ethylene/ethane mixtures with silver zeolite A. *J. Am. Chem. Soc.* **134**, 14635–14637 (2012). [doi:10.1021/ja305663k](https://doi.org/10.1021/ja305663k) [Medline](#)
9. E. D. Bloch, W. L. Queen, R. Krishna, J. M. Zadrozny, C. M. Brown, J. R. Long, Hydrocarbon separations in a metal-organic framework with open iron(II) coordination sites. *Science* **335**, 1606–1610 (2012). [doi:10.1126/science.1217544](https://doi.org/10.1126/science.1217544) [Medline](#)
10. Y. He, R. Krishna, B. Chen, Metal-organic frameworks with potential for energy-efficient adsorptive separation of light hydrocarbons. *Energy Environ. Sci.* **5**, 9107–9120 (2012).
[doi:10.1039/c2ee22858k](https://doi.org/10.1039/c2ee22858k)
11. B. Li, Y. Zhang, R. Krishna, K. Yao, Y. Han, Z. Wu, D. Ma, Z. Shi, T. Pham, B. Space, J. Liu, P. K. Thallapally, J. Liu, M. Chrzanowski, S. Ma, Introduction of π -complexation into porous aromatic framework for highly selective adsorption of ethylene over ethane. *J. Am. Chem. Soc.* **136**, 8654–8660 (2014). [doi:10.1021/ja502119z](https://doi.org/10.1021/ja502119z) [Medline](#)
12. S. Yang, A. J. Ramirez-Cuesta, R. Newby, V. Garcia-Sakai, P. Manuel, S. K. Callear, S. I. Campbell, C. C. Tang, M. Schröder, Supramolecular binding and separation of hydrocarbons within a functionalized porous metal-organic framework. *Nat. Chem.* **7**, 121–129 (2015). [doi:10.1038/nchem.2114](https://doi.org/10.1038/nchem.2114) [Medline](#)
13. C. Güçüyener, J. van den Bergh, J. Gascon, F. Kapteijn, Ethane/ethene separation turned on its head: Selective ethane adsorption on the metal-organic framework ZIF-7 through a gate-opening mechanism. *J. Am. Chem. Soc.* **132**, 17704–17706 (2010).
[doi:10.1021/ja1089765](https://doi.org/10.1021/ja1089765) [Medline](#)

14. A. Mersmann, B. Fill, R. Hartmann, S. Maurer, The potential of energy saving by gas-phase adsorption processes. *Chem. Eng. Technol.* **23**, 937–944 (2000). [doi:10.1002/1521-4125\(200011\)23:11<937:AID-CEAT937>3.0.CO;2-P](https://doi.org/10.1002/1521-4125(200011)23:11<937:AID-CEAT937>3.0.CO;2-P)
15. T. Ren, M. Patel, K. Blok, Olefins from conventional and heavy feedstocks: Energy use in steam cracking and alternative processes. *Energy* **31**, 425–451 (2006). [doi:10.1016/j.energy.2005.04.001](https://doi.org/10.1016/j.energy.2005.04.001)
16. H. Furukawa, K. E. Cordova, M. O’Keeffe, O. M. Yaghi, The chemistry and applications of metal-organic frameworks. *Science* **341**, 1230444 (2013). [doi:10.1126/science.1230444](https://doi.org/10.1126/science.1230444) [Medline](#)
17. H. Sato, W. Kosaka, R. Matsuda, A. Hori, Y. Hijikata, R. V. Belosludov, S. Sakaki, M. Takata, S. Kitagawa, Self-accelerating CO sorption in a soft nanoporous crystal. *Science* **343**, 167–170 (2014). [doi:10.1126/science.1246423](https://doi.org/10.1126/science.1246423) [Medline](#)
18. A. Cadiou, K. Adil, P. M. Bhatt, Y. Belmabkhout, M. Eddaoudi, A metal-organic framework-based splitter for separating propylene from propane. *Science* **353**, 137–140 (2016). [doi:10.1126/science.aaf6323](https://doi.org/10.1126/science.aaf6323) [Medline](#)
19. R. Vaidhyanathan, S. S. Iremonger, G. K. H. Shimizu, P. G. Boyd, S. Alavi, T. K. Woo, Direct observation and quantification of CO₂ binding within an amine-functionalized nanoporous solid. *Science* **330**, 650–653 (2010). [doi:10.1126/science.1194237](https://doi.org/10.1126/science.1194237) [Medline](#)
20. P. Nugent, Y. Belmabkhout, S. D. Burd, A. J. Cairns, R. Luebke, K. Forrest, T. Pham, S. Ma, B. Space, L. Wojtas, M. Eddaoudi, M. J. Zaworotko, Porous materials with optimal adsorption thermodynamics and kinetics for CO₂ separation. *Nature* **495**, 80–84 (2013). [doi:10.1038/nature11893](https://doi.org/10.1038/nature11893) [Medline](#)
21. Q.-G. Zhai, X. Bu, C. Mao, X. Zhao, L. Daemen, Y. Cheng, A. J. Ramirez-Cuesta, P. Feng, An ultra-tunable platform for molecular engineering of high-performance crystalline porous materials. *Nat. Commun.* **7**, 13645 (2016). [doi:10.1038/ncomms13645](https://doi.org/10.1038/ncomms13645) [Medline](#)
22. K. Li, D. H. Olson, J. Seidel, T. J. Emge, H. Gong, H. Zeng, J. Li, Zeolitic imidazolate frameworks for kinetic separation of propane and propene. *J. Am. Chem. Soc.* **131**, 10368–10369 (2009). [doi:10.1021/ja9039983](https://doi.org/10.1021/ja9039983) [Medline](#)
23. W. Liang, F. Xu, X. Zhou, J. Xiao, Q. Xia, Y. Li, Z. Li, Ethane selective adsorbent Ni(bdc)(ted)_{0.5} with high uptake and its significance in adsorption separation of ethane and ethylene. *Chem. Eng. Sci.* **148**, 275–281 (2016). [doi:10.1016/j.ces.2016.04.016](https://doi.org/10.1016/j.ces.2016.04.016)
24. Y. Chen, Z. Qiao, H. Wu, D. Lv, R. Shi, Q. Xia, J. Zhou, Z. Li, An ethane-trapping MOF PCN-250 for highly selective adsorption of ethane over ethylene. *Chem. Eng. Sci.* **175**, 110–117 (2018). [doi:10.1016/j.ces.2017.09.032](https://doi.org/10.1016/j.ces.2017.09.032)
25. D. J. Xiao, E. D. Bloch, J. A. Mason, W. L. Queen, M. R. Hudson, N. Planas, J. Borycz, A. L. Dzubak, P. Verma, K. Lee, F. Bonino, V. Crocellà, J. Yano, S. Bordiga, D. G. Truhlar, L. Gagliardi, C. M. Brown, J. R. Long, Oxidation of ethane to ethanol by N₂O in a metal-organic framework with coordinatively unsaturated iron(II) sites. *Nat. Chem.* **6**, 590–595 (2014). [doi:10.1038/nchem.1956](https://doi.org/10.1038/nchem.1956) [Medline](#)
26. Z. Li, A. W. Peters, A. E. Platero-Prats, J. Liu, C.-W. Kung, H. Noh, M. R. DeStefano, N. M. Schweitzer, K. W. Chapman, J. T. Hupp, O. K. Farha, Fine-tuning the activity of metal-

organic framework-supported cobalt catalysts for the oxidative dehydrogenation of propane. *J. Am. Chem. Soc.* **139**, 15251–15258 (2017). [doi:10.1021/jacs.7b09365](https://doi.org/10.1021/jacs.7b09365) [Medline](#)

27. J. Cho, S. Jeon, S. A. Wilson, L. V. Liu, E. A. Kang, J. J. Braymer, M. H. Lim, B. Hedman, K. O. Hodgson, J. S. Valentine, E. I. Solomon, W. Nam, Structure and reactivity of a mononuclear non-haem iron(III)-peroxo complex. *Nature* **478**, 502–505 (2011). [doi:10.1038/nature10535](https://doi.org/10.1038/nature10535) [Medline](#)
28. E. D. Bloch, L. J. Murray, W. L. Queen, S. Chavan, S. N. Maximoff, J. P. Bigi, R. Krishna, V. K. Peterson, F. Grandjean, G. J. Long, B. Smit, S. Bordiga, C. M. Brown, J. R. Long, Selective binding of O₂ over N₂ in a redox-active metal-organic framework with open iron(II) coordination sites. *J. Am. Chem. Soc.* **133**, 14814–14822 (2011). [doi:10.1021/ja205976v](https://doi.org/10.1021/ja205976v) [Medline](#)
29. W. L. Queen, E. D. Bloch, C. M. Brown, M. R. Hudson, J. A. Mason, L. J. Murray, A. J. Ramirez-Cuesta, V. K. Peterson, J. R. Long, Hydrogen adsorption in the metal-organic frameworks Fe₂(dobdc) and Fe₂(O₂)(dobdc). *Dalton Trans.* **41**, 4180–4187 (2012). [doi:10.1039/c2dt12138g](https://doi.org/10.1039/c2dt12138g) [Medline](#)
30. L. J. Murray, M. Dinca, J. Yano, S. Chavan, S. Bordiga, C. M. Brown, J. R. Long, Highly-selective and reversible O₂ binding in Cr₃(1,3,5-benzenetricarboxylate)₂. *J. Am. Chem. Soc.* **132**, 7856–7857 (2010). [doi:10.1021/ja1027925](https://doi.org/10.1021/ja1027925) [Medline](#)
31. J. Kim, L.-C. Lin, R. L. Martin, J. A. Swisher, M. Haranczyk, B. Smit, Large-scale computational screening of zeolites for ethane/ethene separation. *Langmuir* **28**, 11914–11919 (2012). [doi:10.1021/la302230z](https://doi.org/10.1021/la302230z) [Medline](#)
32. L. Li, R.-B. Lin, R. Krishna, X. Wang, B. Li, H. Wu, J. Li, W. Zhou, B. Chen, Flexible-robust metal-organic framework for efficient removal of propyne from propylene. *J. Am. Chem. Soc.* **139**, 7733–7736 (2017). [doi:10.1021/jacs.7b04268](https://doi.org/10.1021/jacs.7b04268) [Medline](#)
33. R. A. Meyers, *Handbook of Petrochemicals Production Processes* (McGraw-Hill, 2005).
34. P. Giannozzi, S. Baroni, N. Bonini, M. Calandra, R. Car, C. Cavazzoni, D. Ceresoli, G. L. Chiarotti, M. Cococcioni, I. Dabo, A. Dal Corso, S. de Gironcoli, S. Fabris, G. Fratesi, R. Gebauer, U. Gerstmann, C. Gougaussis, A. Kokalj, M. Lazzeri, L. Martin-Samos, N. Marzari, F. Mauri, R. Mazzarello, S. Paolini, A. Pasquarello, L. Paulatto, C. Sbraccia, S. Scandolo, G. Sclauzero, A. P. Seitsonen, A. Smogunov, P. Umari, R. M. Wentzcovitch, QUANTUM ESPRESSO: A modular and open-source software project for quantum simulations of materials. *J. Phys. Condens. Matter* **21**, 395502 (2009). [doi:10.1088/0953-8984/21/39/395502](https://doi.org/10.1088/0953-8984/21/39/395502) [Medline](#)
35. V. Barone, M. Casarin, D. Forrer, M. Pavone, M. Sambi, A. Vittadini, Role and effective treatment of dispersive forces in materials: Polyethylene and graphite crystals as test cases. *J. Comput. Chem.* **30**, 934–939 (2009). [doi:10.1002/jcc.21112](https://doi.org/10.1002/jcc.21112) [Medline](#)
36. Y. He, Z. Zhang, S. Xiang, F. R. Fronczek, R. Krishna, B. Chen, A microporous metal-organic framework for highly selective separation of acetylene, ethylene, and ethane from methane at room temperature. *Chemistry* **18**, 613–619 (2012). [doi:10.1002/chem.201102734](https://doi.org/10.1002/chem.201102734) [Medline](#)

37. Y. He, Z. Zhang, S. Xiang, F. R. Fronczek, R. Krishna, B. Chen, A robust doubly interpenetrated metal-organic framework constructed from a novel aromatic tricarboxylate for highly selective separation of small hydrocarbons. *Chem. Commun.* **48**, 6493–6495 (2012). [doi:10.1039/c2cc31792c](https://doi.org/10.1039/c2cc31792c) [Medline](#)
38. Y. Wu, H. Chen, D. Liu, Y. Qian, H. Xi, Adsorption and separation of ethane/ethylene on ZIFs with various topologies: Combining GCMC simulation with the ideal adsorbed solution theory (IAST). *Chem. Eng. Sci.* **124**, 144–153 (2015).
[doi:10.1016/j.ces.2014.07.019](https://doi.org/10.1016/j.ces.2014.07.019)
39. D.-L. Chen, N. Wang, C. Xu, G. Tu, W. Zhu, R. Krishna, A combined theoretical and experimental analysis on transient breakthroughs of C₂H₆/C₂H₄ in fixed beds packed with ZIF-7. *Microporous Mesoporous Mater.* **208**, 55–65 (2015).
[doi:10.1016/j.micromeso.2015.01.019](https://doi.org/10.1016/j.micromeso.2015.01.019)
40. J. Pires, M. L. Pinto, V. K. Saini, Ethane selective IRMOF-8 and its significance in ethane-ethylene separation by adsorption. *ACS Appl. Mater. Interfaces* **6**, 12093–12099 (2014).
[doi:10.1021/am502686g](https://doi.org/10.1021/am502686g) [Medline](#)